Article

Structural variants drive context-dependent oncogene activation in cancer

https://doi.org/10.1038/s41586-022-05504-4

Received: 21 September 2020

Accepted: 1 November 2022

Published online: 07 December 2022

Check for updates

Zhichao Xu[1,6], Dong-Sung Lee[2,6], Sahaana Chandran[1], Victoria T. Le[1], Rosalind Bump[1], Jean Yasis[1], Sofia Dallarda[1], Samantha Marcotte[1], Benjamin Clock[1], Nicholas Haghani[1], Chae Yun Cho[1], Kadir C. Akdemir[3,4], Selene Tyndale[5], P. Andrew Futreal[3], Graham McVicker[5], Geoffrey M. Wahl[1] & Jesse R. Dixon[1] ✉

Higher-order chromatin structure is important for the regulation of genes by distal regulatory sequences[1,2]. Structural variants (SVs) that alter three-dimensional (3D) genome organization can lead to enhancer–promoter rewiring and human disease, particularly in the context of cancer[3]. However, only a small minority of SVs are associated with altered gene expression[4,5], and it remains unclear why certain SVs lead to changes in distal gene expression and others do not. To address these questions, we used a combination of genomic profiling and genome engineering to identify sites of recurrent changes in 3D genome structure in cancer and determine the effects of specific rearrangements on oncogene activation. By analysing Hi-C data from 92 cancer cell lines and patient samples, we identified loci affected by recurrent alterations to 3D genome structure, including oncogenes such as *MYC*, *TERT* and *CCND1*. By using CRISPR–Cas9 genome engineering to generate de novo SVs, we show that oncogene activity can be predicted by using 'activity-by-contact' models that consider partner region chromatin contacts and enhancer activity. However, activity-by-contact models are only predictive of specific subsets of genes in the genome, suggesting that different classes of genes engage in distinct modes of regulation by distal regulatory elements. These results indicate that SVs that alter 3D genome organization are widespread in cancer genomes and begin to illustrate predictive rules for the consequences of SVs on oncogene activation.

The three-dimensional (3D) organization of the genome is a critical feature for gene regulation by distal enhancers[1,2,6]. Recently, both germline and somatic mutations that alter 3D genome structure have been discovered that rewire enhancer–promoter communication and alter gene expression in human disease[3], a process often termed 'enhancer hijacking'. Such regulatory rewiring has long been recognized as a potential mechanism for activation of oncogenes in cancer[7,8] and has more recently been identified acting at genes such as *IGF2* (ref. [9]), *GFI1* (ref. [10]), *TERT*[11], *MECOM*[12] and *TAL1* (ref. [13]) in specific cancer types. In addition, recent tools have been developed to directly identify enhancer hijacking events from Hi-C datasets in cancer genomes[14]. Apart from structural mutations, *trans*-acting epigenetic rewiring has also been identified as a mechanism leading to the activation of *PDGFRA*[15] and *FGF4* (ref. [16]). Taken together, these observations suggest a growing recognition of enhancer hijacking as a mechanism for oncogene activation.

Despite our increasing appreciation of the role of structural variants (SVs) in leading to enhancer hijacking, more recent studies have shown that, in fact, few SVs actually lead to changes in nearby expression of genes. Specifically, studies examining highly rearranged 'balancer' chromosomes in *Drosophila* or examining SVs from thousands of patient tumour samples have shown that the vast majority of SVs appear to have no discernable impact on expression of neighbouring genes[4,5]. As a result, it is currently unclear what distinguishes SVs that lead to phenotypic consequences by changing nearby gene expression from those that do not.

To address these challenges, we generated Hi-C data for 58 cancer cell lines or patient samples and re-analysed public Hi-C data for 34 cancer cell lines or patient samples. By using tools for identifying SVs from Hi-C data, we have identified 4,543 SVs across all 92 samples. We also developed computational tools to classify whether rearrangements result in the formation of new topologically associating domains (TADs). We identify multiple loci affected by recurrent regulatory 3D genome alterations in diverse cancer types, including the *MYC*, *TERT* and *CCND1* genes. By examining SV data from patient whole-genome sequencing studies, we observe that these loci are associated with an increased frequency of rearrangements between TADs and, in some cases, are associated with a worse prognosis.

We also analysed patterns of RNA-seq data from patient samples associated with SVs and observed that, even at sites of recurrent structural variation, there were highly heterogeneous effects on the expression of nearby genes. To better understand the molecular basis for this, we used CRISPR–Cas9 technology to engineer SVs de novo into cell

[1]Gene Expression Laboratory; Salk Institute for Biological Studies, La Jolla, CA, USA. [2]Department of Life Sciences, University of Seoul, Seoul, South Korea. [3]Department of Genomic Medicine, UT MD Anderson Cancer Center, Houston, TX, USA. [4]Department of Neurosurgery, UT MD Anderson Cancer Center, TX, Houston, USA. [5]Integrative Biology Laboratory; Salk Institute for Biological Studies, La Jolla, CA, USA. [6]These authors contributed equally: Zhichao Xu, Dong-Sung Lee. ✉e-mail: jedixon@salk.edu

lines. These experiments indicate that the likelihood of activation of an oncogene is associated with the 'enhancer load' and 3D genome conformation of the partner region and can be predicted by using models that integrate these features, such as activity-by-contact (ABC) models. Critically, the expression of only a subset of genes is sensitive to these engineered rearrangements, and we observe that only a minority of genes in the genome show evidence of responsiveness to changes in their local enhancer landscape. These results indicate that alterations to gene regulatory 3D architecture are a critical mechanism that enables oncogene activation in cancer genomes and sheds light on the essential elements for such gene activation events.

Discovery of SVs by using Hi-C data

To study the effects of structural variation on 3D genome organization in cancer genomes, we generated Hi-C datasets for 58 cancer cell lines or primary patient tumour samples (48 cancer cell lines, 10 patient tumour samples) and combined these with 34 publicly available datasets (Fig. 1a)[5,17–25]. Seventeen of the samples were from patient tumour samples and the rest (75) were from cancer cell lines (Supplementary Table 1). The Hi-C libraries were sequenced such that the median sample contained 116 million contacts, sufficient for analysing genomic features such as TADs and SVs.

To identify SVs that impact 3D genome structure, we utilized our recently developed method, hic-breakfinder[17]. As we and others have observed, the presence of SVs leads to large deviations in Hi-C data in the vicinity of the SV breakpoint (Fig. 1b)[17,19,26–29]. This signal can be used to identify SVs from Hi-C data, although it is biased toward identifying large (more than 1 Mb) SVs. We identified a total of 4,543 SVs at 1 kb resolution across all 92 samples (Supplementary Table 2), with a median of 33 SVs per sample (Extended Data Fig. 1a,b). To evaluate the sensitivity of our SV calls, we included 10 samples with known disease-defining translocations and were able to identify the known events in 10 of 10 samples (Extended Data Fig. 1c–e). We also evaluated sensitivity by using fusion genes called from RNA-seq data[30–32], and were able to identify 76% (16 of 21) of interchromosomal (reads per kilobase per million reads sequenced (RPKM) > 1) and 60% (12 of 20) of large (more than 1 Mb, RPKM > 1) fusion genes. In summary, these results indicate that our Hi-C-based SV call set is sensitive to large structural rearrangements across the samples we profiled.

We next examined the distribution of SVs in our dataset. We observed slightly more interchromosomal versus intrachromosomal rearrangements (Extended Data Fig. 2a). However, a subset of samples showed markedly elevated frequencies of intrachromosomal rearrangements (Extended Data Fig. 2b), reminiscent of complex chromosomal rearrangements such as chromothripsis or chromoplexy[33,34]. We identified chromosomes affected by these focal rearrangements by comparing chromosome-specific breakpoint occurrences with the genome-wide frequency in a given sample (see Methods for details). We identified 38 cases of chromosomes showing high-frequency rearrangement clusters in 34% of samples (32 of 92) (Extended Data Fig. 2c,d), similar to estimates of the frequency of chromothripsis derived from whole-genome sequencing samples (29%)[35]. For example, the SNU-C1 colon cancer cell line has been previously described as having a chromothripsis event on chromosome 15 (ref. [36]). We observed extensive rearrangement of the entire chromosome 15 of the SNU-C1 colon cancer cell (Extended Data Fig. 2e, upper right) that is not present in other colon cancer samples (Extended Data Fig. 2e, lower left). In summary, we have assembled a large Hi-C dataset that provides a rich resource for the investigation of SVs and 3D genome structure in cancer genomes.

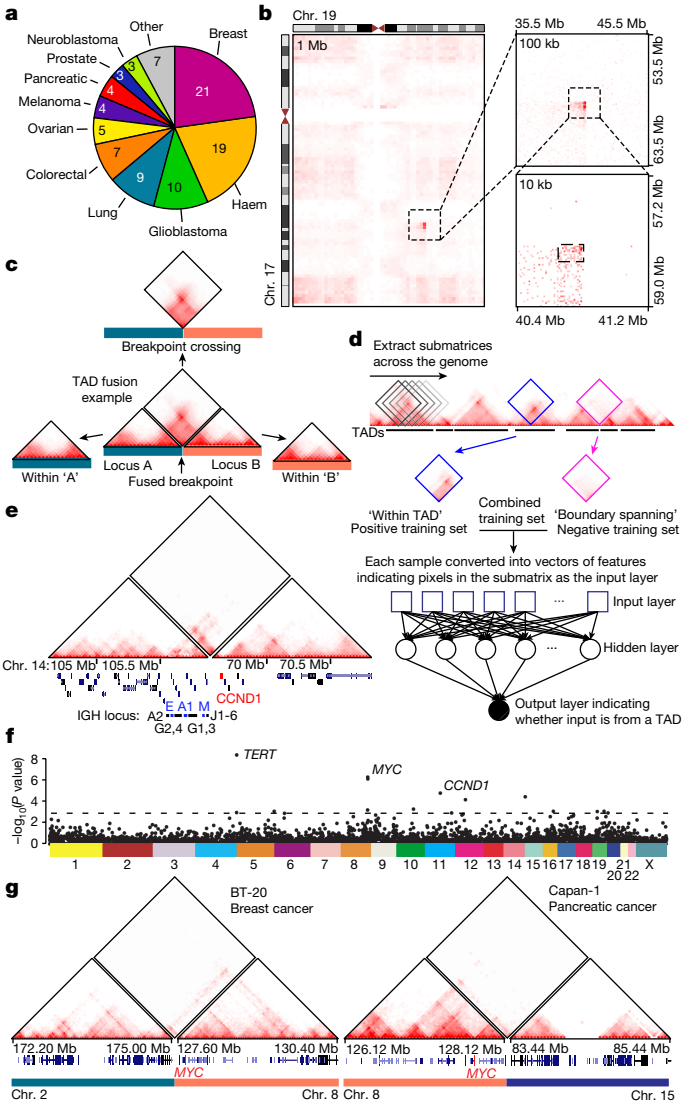

Fig. 1 | TAD fusion events from Hi-C data in cancer samples. a, Tumour types represented in 92 cancer cell lines and patient tumour samples Hi-C datasets. **b**, Translocation between chromosomes 17 and 19 from a breast cancer patient tumour sample (C3-14_06). Translocations are first identified from chromatin interactions at low resolutions (1 Mb, left heat map) and progressively refined at higher resolutions (right heat maps). **c**, Strategy of identifying TAD fusion events in rearranged genomes. An example TAD fusion event is between two otherwise distal loci ('locus A' and 'locus B'). The chromatin interactions can be broken down into those that occur within the breakpoint proximal regions (triangle heat maps, 'within A' or 'within B') and those that cross the breakpoint (diamond heat map). **d**, Neural-network-based classifier for identifying TAD fusion events. 'Diamond' matrices from non-rearranged regions within TADs or between TADs are used to train the neural-network model. The model then classifies a diamond matrix from a SV as derived from a TAD or not. **e**, Hi-C data from an *IGH–CCND1* fusion in the Granta cell line predicted to form a TAD fusion event. The left-hand triangle heat map shows interactions within chromosome 14, the right-hand triangle heat map shows interactions within chromosome 11 and the diamond heat map shows interactions crossing the breakpoint between chromosomes 11 and 14. *IGH* and *CCND1* loci are marked at the bottom. **f**, The *P* value for the number of TAD fusion events for each TAD in the genome. The *P* value is computed with a null model that considers the overall frequency of TAD fusion events and the size of each domain. The dashed line represents the threshold for an FDR of less than 20%. **g**, Examples of identified TAD fusion events at the *MYC* locus in two cell lines.

Neural networks to identify TAD fusions

Having identified SVs from Hi-C data, we wanted to determine whether these events caused the formation of neo-TADs. Numerous computational tools have been described to identify TADs in Hi-C data[37], but they assume a contiguous linear genome and are unsuitable for rearranged genomes. Therefore, we designed a neural-network

classifier to determine whether Hi-C data crossing a SV breakpoint form a new TAD (Fig. 1c,d). This method is trained by using non-rearranged regions of the genome based on annotations from standard TAD calling algorithms (Fig. 1d). By using cross-validation, we observed high accuracy (median = 93.5%) and low false discovery rate (FDR) (median = 6.15%) when applied to the 82 Hi-C datasets with sufficient coverage for TAD-based analysis (Extended Data Fig. 2f).

We then applied the classifier across our Hi-C samples and classified 80.7% of SVs as forming a TAD fusion event, indicating that most rearrangements create new breakpoints crossing TADs. This high frequency of TAD fusion events is consistent with fusion TADs forming by co-opting 'loop extrusion'[38] to fuse the nearest breakpoint proximal TAD boundaries into a neo-TAD. We next tested whether our method detects known instances of enhancer hijacking events in our samples. In 5 of 5 Mantle cell lymphoma samples that contain known *IGH–CCND1* rearrangements[39], our classifier identified TAD fusion events at the *CCND1* locus (Fig. 1e). Furthermore, we identified TAD fusion events at the *TERT* gene in one out of three neuroblastoma samples (SK-N-AS), consistent with the frequency of TERT rearrangements observed in patient samples (31%)[11]. Taken together, these results validate that our classifier can identify new breakpoint crossing enhancer–gene interactions.

We observed that TAD fusion events are enriched for oncogenes (Extended Data Fig. 2g), suggesting that these events may be associated with functional consequences. We also observed that rearranged TADs are more likely to contain active enhancers and super-enhancers (Extended Data Fig. 2h–j). This does not appear to result from increased fragility, as double-strand break sequencing[40] shows no enrichment of double-strand breaks in TADs containing super-enhancers (Extended Data Fig. 2k). A possible explanation for these findings is that TAD fusion events that contain super-enhancers are more likely to induce altered gene expression and confer an oncogenic growth advantage if linked to pro-growth genes.

Recurrent TAD fusions in cancer genomes

Having identified TAD fusion events in cancer cell lines and patient samples, we tested whether any loci showed evidence of recurrent TAD fusions. TADs are largely conserved across cell types[41,42], but some boundaries are cell type specific[43]. To account for cell-type variable TAD boundaries, we identified TADs in five samples (human embryonic stem cells (hESCs)[44], DLD-1, HCC38, MV411 and NCI-H1437) representing both non-malignant (hESC) and malignant samples from diverse tumour types. Taking the union of TAD boundaries across these five samples yielded a set of 5,450 domains (Extended Data Fig. 3a).

We then quantified the frequency of TAD fusions across 82 samples accounting for the genome-wide frequency of TAD fusions and domain size (see Methods for details). We identified six loci showing recurrent TAD fusions under a FDR of 5% and 16 loci with evidence under an FDR of 20% (Fig. 1f, Extended Data Fig. 3b and Supplementary Table 2). Several well-known oncogenes are found within these TADs, including *MYC*, *TERT* and *CCND1*. Collectively, 46% (38 of 82) of cell lines or patient samples have a TAD fusion at one of these 16 loci, suggesting that recurrent TAD fusion events are common in cancer genomes. These results also represent a baseline for the number of loci affected by 3D genome alterations, and studies with more extensive and diverse samples will probably detect additional loci.

MYC has been shown to contact numerous regulatory elements over an approximately 3 Mb sized TAD[45–47]. In our merged TAD call set, this domain is split into four subdomains (Extended Data Fig. 3c). Both the immediate upstream and downstream sub-TADs are enriched for rearrangements (upstream $P = 5.96 \times 10^{-7}$, downstream $P = 8.7 \times 10^{-7}$, permutation test). When considering the entire approximately 3 Mb domain together, the locus surrounding *MYC* is most frequently affected in our dataset (20.7% or 17 of 82 samples). *MYC* is known to undergo copy number changes[48], but most of the rearrangements we identified were not accompanied by high-level (more than 6*N*) copy number changes (Extended Data Fig. 3d). Similarly, *MYC* is the target of rearrangements in haematopoietic malignancies[49], but we observed TAD fusion events in diverse cancer types, including breast, osteosarcoma, neuroblastoma, lymphoma and pancreatic cancer (Fig. 1g and Extended Data Fig. 3e,f). Together, these results indicate that TAD fusions affecting multiple well-known oncogenes are common in cancer genomes.

MYC rearrangements in patient samples

Having identified loci with recurrent TAD fusion events in cancer cell lines, we tested whether these loci also show frequent rearrangements in 2,510 tumour samples profiled by the Pan-Cancer Analysis of Whole Genomes–International Cancer Genome Consortium (PCAWG–ICGC)[50]. As our Hi-C data suggested that most SVs between different TADs result in a TAD fusion, we focused our analysis on SVs for which the two break ends map within different TADs (Fig. 2a). We quantified the frequency of rearrangements per TAD after lifting over the union TAD calls to the hg19 genome (15 of 16 successfully lifted over). We found 10 of 15 of these TADs show recurrent inter-TAD rearrangements in the PCAWG–ICGC data (FDR = 5%; Fig. 2a).

As in our observations based on Hi-C data, the upstream and downstream subdomains at the *MYC* locus were enriched for inter-TAD rearrangements (Fig. 2a), and the previously described single approximately 3 Mb domain[45] was frequently rearranged in diverse cancer types (Extended Data Fig. 4a). The overall frequency of rearrangements across the approximately 3 Mb *MYC* domain (8.96%, 225 of 2,510) is lower than the frequency observed in our Hi-C dataset (20.7%, 17 of 82), potentially reflecting differences in cell lines or tumour type. RNA-sequencing data from matched patient tumour samples showed that samples with rearrangements within the *MYC* domain have higher levels of *MYC* expression (Fig. 2b). Across all tumour types, the breakpoints for most (94.8%) inter-TAD rearrangements were distal (more than 10 kb) from the *MYC* transcription start site, including those associated with elevated *MYC* expression (Fig. 2b). *MYC* expression is elevated in different tumour types (Fig. 2c), indicating that the pan-cancer differences in expression are not due to a single affected tumour type.

MYC is frequently amplified in many tumour types[48], and we explored whether the changes in *MYC* expression could be explained by SVs, copy number changes or both. Samples with copy number gains of *MYC* are more likely to contain SVs (Extended Data Fig. 4b), probably due to unbalanced translocations or tandem duplications. For samples that lack SVs, *MYC* expression increases with increasing copy number, as expected based on 'gene dosage'. However, samples containing SVs display elevated *MYC* expression regardless of copy number (Extended Data Fig. 4c), suggesting that SVs that rewire the *MYC* domain can lead to increased expression regardless of gene dosage. For example, *MYC* expression is still elevated in tumours that lack high-level amplifications (Extended Data Fig. 4d) and in tumours without any changes in copy number (Extended Data Fig. 4e). Furthermore, some tumour types also show lower overall survival for patients with inter-TAD rearrangements at the *MYC* domain (Fig. 2d, Supplementary Table 3), indicating that these rearrangements may portend a worse prognosis.

Rearrangements can occur throughout the TAD surrounding *MYC*, including occurring more than 1 Mb away from the *MYC* gene (Extended Data Fig. 4f). Examining Hi-C data from normal cell lines[20,44], the *MYC* locus shows notable cell-type-specific chromatin interactions with distal regulatory sequences for over 1–2 Mb (Fig. 2e), potentially enabling the *MYC* to contact many distal regulatory sequences, as has been recently suggested[45]. This suggests that *MYC* may be uniquely susceptible to dysregulation by distal regulatory rearrangements.

Examining the partner regions of *MYC*, we found 285 unique partner TADs in the 225 patients containing inter-TAD rearrangements at the

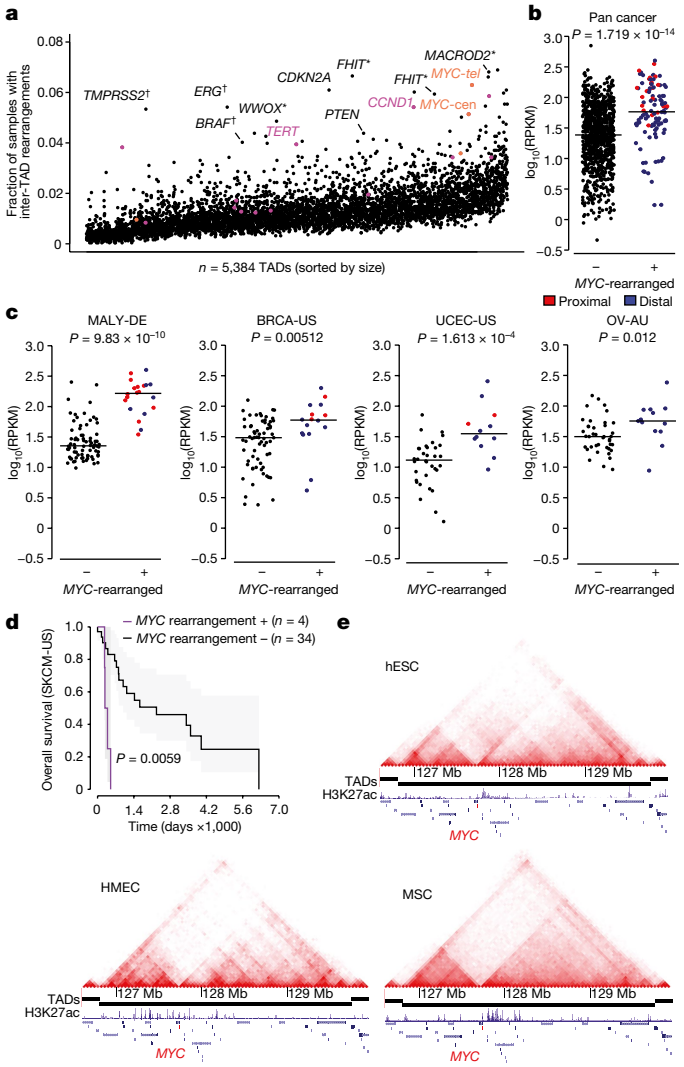

Fig. 2 | Interdomain rearrangements in patient tumour samples. a, The frequency of inter-TAD rearrangements among 2,510 patient samples for each of 5,384 domains across the genome (5,384 of 5,450 domains successfully lifted over to hg19 genome). Domains are sorted by size. The four subdomains near the *MYC* gene are labelled in orange. The subdomains immediately upstream (centromeric) or downstream (telomeric) of *MYC* are labelled '*MYC*-cen' and '*MYC*-tel', respectively. Select domains are also labelled by gene names within each domain. Genes at known fragile sites are labelled with an asterisk, and genes at known high-frequency gene fusion events are labelled with a dagger. Domains that show frequent TAD fusion events based on Hi-C data are shown in pink with the exception of the *MYC*-cen and *MYC*-tel domains. **b**, Expression level of the *MYC* gene based on RNA-seq in matched patient samples for tumours that do not contain inter-TAD rearrangements at the *MYC* TAD (non-rearranged) or that do contain inter-TAD rearrangements at the *MYC* locus (MYC-rearranged). Results are shown for all patients with matching SV and RNA-seq data (Pan cancer). The *P* value is from a two-sided Wilcoxon rank sum test. **c**, As in **b**, but showing expression for specific tumour subsets (MALY-DE, malignant lymphoma; BRCA-US, breast cancer; UCEC-US, endometrial cancer; OV-AU, ovarian cancer; abbreviations based on the PCAWG of whole genomes naming conventions). The *P* value is from a two-sided Wilcoxon rank sum test. **d**, Kaplan–Meier survival curves for patients in a melanoma cohort (SKCM-US) separated into those with inter-TAD rearrangements at the *MYC* locus (purple, $n = 4$) and those without (grey, $n = 34$). The *P* value is from a two-sided Cox proportional hazard model likelihood ratio test. **e**, Hi-C data over the TAD containing the *MYC* gene in H1 hESCs, human mammary epithelial cells (HMECs) and mesenchymal stem cells (MSCs). Shown below the tracks are ChIP–seq data for H3K27ac in each lineage.

MYC locus. We did not observe any rearrangement partner in more than 5% of patient samples (Extended Data Fig. 4f and Supplementary Table 4), in contrast with what is known to occur in *IGH–MYC* rearrangements in lymphomas. The most frequently rearranged partners were immediately adjacent to the *MYC* domain, consistent with SVs occurring more frequently between regions in close spatial proximity[51]. The majority (223 of 285) of partner TADs are found in only one patient. These results indicate that although the *MYC* domain is highly enriched for inter-TAD rearrangements, these rearrangements are not dominated by specific partner regions. This regulatory rewiring of the *MYC* locus, in addition to previously well-described copy number amplifications and activation of endogenous *MYC* super-enhancers, represents multiple roads that cancer cells will use to activate the *MYC* gene.

Generation of de novo translocations

Genetic and cytogenetic features of tumours are frequently used to guide the staging, prognosis and treatment of cancer patients[52,53]. However, it is challenging to determine whether an individual SV causes *MYC* activation as *MYC* expression is highly heterogeneous in samples with SVs in the *MYC* TAD (Fig. 2b), and we do not observe specific pan-cancer partner regions (Extended Data Fig. 4f and Supplementary Table 4). These observations, taken together with recent studies indicating that only a minority of SVs are associated with changes in gene expression[4,5], indicate that it is difficult to predict whether a given SV will drive *MYC* expression from the genomic sequence alone. This limits our ability to predict whether a given SV will have a functional impact in an individual patient tumour sample.

To better understand what rearrangements induce *MYC* expression, we performed CRISPR–Cas9 engineering[54] to generate de novo translocations from diverse partner regions in a neuroblastoma cell line (SK-N-DZ) that lacks *MYC* expression (Extended Data Fig. 5a,b). We chose neuroblastoma cell lines for this analysis because we and others have shown that neuroblastoma cell lines that contain high levels of *MYC* expression have TAD fusions at the *MYC* locus, whereas lines that do not show *MYC* expression lack such events[17,55].

We engineered 37 clonal cell lines containing translocations between the *MYC* locus and 15 distinct genomic loci (Fig. 3a,b). These were performed in two sets, a 'test' set in wild-type SK-N-DZ cells and a 'validation' set in an SK-N-DZ line in which an mClover2 reporter was knocked into the 3′ end of the *MYC* gene. We included partner regions with a wide range of enhancer activities, including domains with weak enhancer activity and domains that contain super-enhancers (Fig. 3c). We also included a partner domain in which a strong boundary separates the junction site and a super-enhancer. We validated clones by breakpoint crossing PCR and Sanger sequencing (Extended Data Fig. 5c). We then confirmed that each clone contained a large-scale rearrangement by using chromosome painting (Fig. 3b and Extended Data Fig. 5d) or directly from Hi-C experiments.

To analyse the 3D genome structure changes in the rearranged clones, we performed Hi-C experiments in each engineered clone. By using our neural-network classifier, we observed that all cases were identified as TAD fusions (Fig. 3d). RNA-sequencing data showed over 500-fold differences in *MYC* expression levels between the least (SK-N-DZ chr. 7 clone #1 and chr. 7 clone #3) and most expressed clones (chr. 1 clone #1) (Fig. 3e), similar to the heterogeneity we observed in patient samples (Fig. 2b). We classified six partner regions as '*MYC* activating' and nine as non-activating by comparing *MYC* expression in replicate clones from the same partner region with the parental non-rearranged cell line (FDR 5%). *MYC* is expressed at lower levels in the engineered clones compared to cell lines that harbour endogenous *MYC* rearrangements. However, the strongest activated clones have *MYC* expression that is comparable to cell lines with endogenous *MYC* rearrangements (Extended Data Fig. 5e). The differences in *MYC* expression between clones cannot be explained by any changes in copy number of the *MYC* gene (Extended

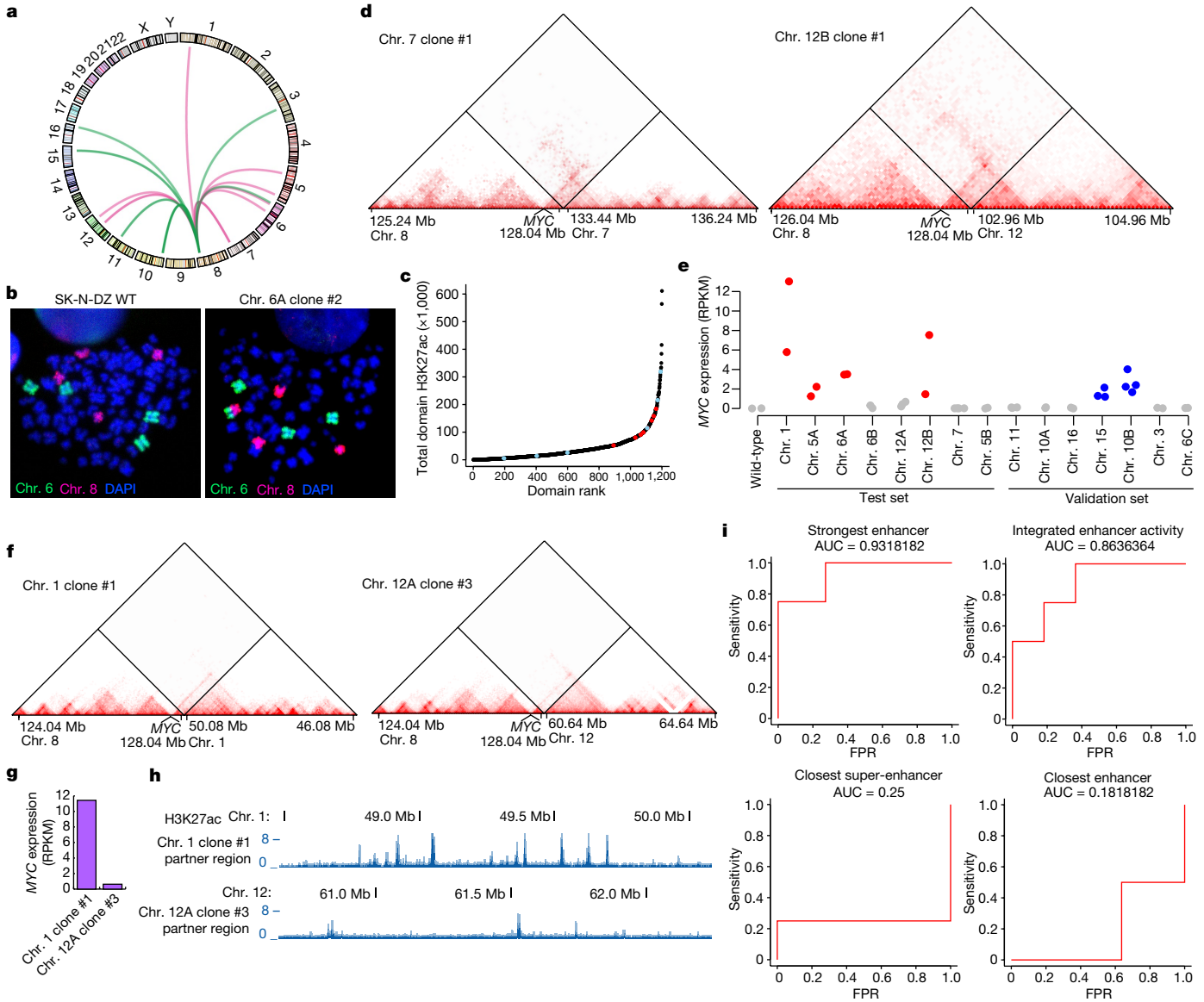

Fig. 3 | Engineered rearrangements and *MYC* gene activation. a, Circos plot of engineered rearrangements. Rearrangements from the test set are red and the validation set are green. **b**, Chromosome painting confirming the presence of a large-scale rearrangement targeting chromosome 6. Chromosome 8 is in red and chromosome 6 is green. DNA is blue by 4′,6-diamidino-2-phenylindole (DAPI) staining. The parent SK-N-DZ cells do not show rearrangements between chromosome 8 and chromosome 6 (left), but translocated chromosomes are observed in the rearranged clones (right). Similar results were observed in a minimum of 20 nuclei for each clone. **c**, Enhancer activity across TADs in SK-N-DZ cells. Enhancers were identified as distal H3K27ac sites based on ChIP–seq data and summed across domains. Domains in the test set are in red, whereas domains in the validation set are in blue. **d**, Hi-C data from two engineered clones showing de novo TAD fusion events to chromosome 7 (left) and chromosome 12 (right). **e**, Expression of the *MYC* gene as measured by RNA-seq in wild-type and engineered SK-N-DZ cells. Clones with *MYC* not activated are coloured grey whereas those with activated *MYC* are coloured red and blue in test and validation set, respectively. **f**, Hi-C data showing an engineered TAD fusion event at the *MYC* locus between chromosome 8 and chromosome 1 (top) and between chromosome 8 and chromosome 12 (bottom). **g**, *MYC* RNA-seq expression in engineered clones shown in **f**. **h**, H3K27ac ChIP–seq signal over the partner region of the engineered rearrangements shown in **f** and **g**. **i**, Receiver operating characteristic (ROC) curves for four models of *MYC* activation. The AUC is also shown for each model. Integrated enhancer activity is calculated by summing all enhancers within 3 Mb of *MYC* over the partner region of the engineered translocation.

Data Fig. 5f), nor any changes in either copy number or expression of the paralogue *MYCN* gene (Extended Data Fig. 5g, h). Therefore, we explored other possible reasons for the observed heterogeneity in *MYC* expression in the engineered clones.

We observed engineered rearrangements with markedly different levels of *MYC* expression showed large differences in the number and strength of distal H3K27ac peaks (Fig. 3f–h), suggesting that the partner region enhancer strength may be related to the heterogeneous effects of TAD fusions on *MYC* expression. To test if partner region enhancer activity contributed to *MYC* expression, we used an SK-N-DZ cell line in which we introduced an mClover2 reporter into the 3′ end of *MYC* and engineered a translocation between chromosome 1 and the *MYC* locus on chromosome 8. As expected, these cells showed high levels of mClover2 expression (Extended Data Fig. 5i). We then deleted the strongest enhancer in the partner region and observed a reduction in mClover2 fluorescence (Extended Data Fig. 5j–l). We next isolated clonal cell lines harbouring the enhancer deletion and determined which allele carried the deletion. Clones with the deletion on the

MYC-translocated chromosome 1 allele have lower *MYC* expression than those with deletion on wild-type chromosome 1 allele (Extended Data Fig. 5m). Although the effects of the enhancer deletion were clear, they are also small, which could be either due to inefficient deletion of the enhancer by the paired guide RNAs (gRNAs) or due to additive effects of multiple enhancers across the partner region contributing to *MYC* expression.

ABC models of engineered rearrangements

Given that *MYC* expression depends on the translocated enhancers, we evaluated whether we could predict *MYC* activation based on the enhancer patterns in the partner region in the test set of engineered clones (Fig. 3e). The distance to the closest enhancer or super-enhancer was a poor predictor (AUC = 0.25 or 0.182), whereas integrating the enhancer signal was a good predictor (Fig. 3i, area under the curve (AUC) = 0.864). Models based on the strongest enhancer performed better (Fig. 3i, AUC = 0.932). However, as deleting the strongest enhancer resulted in only a partial reduction in mClover2 (Extended Data Fig. 5j–m), we reason that the strength of the strongest enhancer is not the primary determinant of *MYC* expression.

In examining our data, one engineered rearrangement for which we placed a strong TAD boundary between the breakpoint and the nearest enhancers was potentially illustrative of the limitations of considering only enhancer activity (Fig. 4a). This rearrangement places a potent super-enhancer (Fig. 4b) approximately 430 kb downstream from the *MYC* gene. However, this rearrangement fails to induce *MYC* expression (Fig. 4c). This suggests that the enhancer strength and how frequently enhancers contact the *MYC* gene contribute to activation. As a result, we considered ABC models[56], in which enhancer activity is integrated across the partner regions but weighted by the interaction frequency of the enhancer with the *MYC* promoter (Extended Data Fig. 6a). This ABC model showed improved predictability (Fig. 4d, AUC = 0.977). We also evaluated a TAD-delimited version of the ABC model that showed similar results (Extended Data Fig. 6b).

Although ABC models are good predictors of *MYC* activation, these models still have limitations. First, although ABC models can determine whether *MYC* is activated, they are not strong predictors of the absolute expression level (Fig. 4e, Pearson correlation = 0.48). A second limitation is that we use experimentally measured Hi-C contact patterns in the rearranged sample. To test whether the ABC models could be predictive without experimental evaluation after the rearrangement, we tested ABC models in which the observed Hi-C contact frequency is replaced with genome-wide averages (Extended Data Fig. 6c) or with predicted contact frequencies from the deep-learning-based tool, Orca[57] (Fig. 4f,g). The ABC models based on inferred contact frequencies performed comparable to or better than models considering the experimentally observed contact frequency (Fig. 4d–g).

Finally, to test how well these models generalized, we identified the most accurate model score in the test set and applied this score to the validation set of clones. The ABC models, in particular ones that explicitly account for TAD boundaries, were the most accurate (accuracy 88%) (Fig. 4h). Taken together, these results indicate that *MYC* expression can be quantitatively predicted by using models of enhancer activity in the partner region. Furthermore, these results may explain part of the heterogeneity in *MYC* expression observed in patient samples and engineered rearrangements.

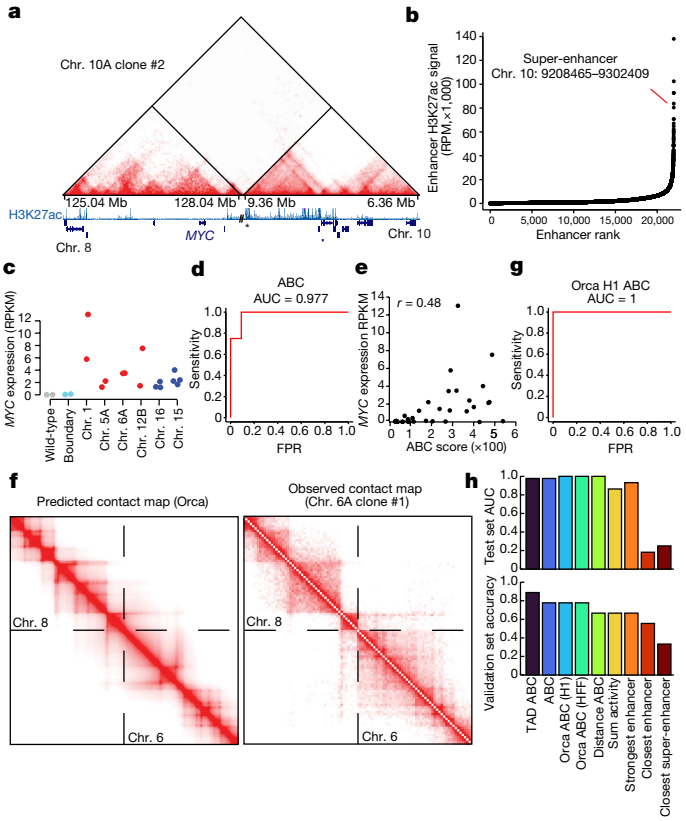

Fig. 4 | Quantitative models of *MYC* expression in the context of engineered rearrangements. a, Hi-C data of an engineered rearrangement between chromosome 8 and 10 for which a strong TAD boundary is located immediately downstream from the breakpoint with a strong super-enhancer distal to the TAD boundary. Below the track is the H3K27ac ChIP–seq signal. An asterisk marks the location of the strong super-enhancer. **b**, Scatter plot of ranked enhancer strength as measured by H3K27ac ChIP–seq. The super-enhancer downstream from the TAD boundary shown in **a** is highlighted in red. **c**, *MYC* expression in engineered clones. The light blue 'boundary' clone is the event shown in **a**, whereas the other clones are instances in which *MYC* shows significant upregulation compared to the parent wild-type SK-N-DZ cell line. **d**, ROC curve for the ABC model. **e**, Scatter plot of the ABC score compared to *MYC* expression as measured by RNA-seq (RPKM). **f**, Predicted (left) and observed (right) contact maps resulting from an engineered translocation between chromosome 6 and 8. **g**, ROC curve for an ABC model for which contacts are replaced by predicted contact frequency from the Orca deep-learning model. **h**, Bar plots showing the AUC for the test set of engineered rearrangements (top) for different predictive models of *MYC* activation as well as the classification accuracy of each model on the validation set of engineered rearrangements. The score for the validation set was chosen as the cut-off from the test set with the highest classification accuracy. HFF, human foreskin fibroblasts.

Identification of ABC-responsive genes

Interestingly, no nearby gene besides *MYC* showed variable expression in response to engineered SVs (Fig. 5a) despite several neighbouring genes having similarly strong variations in ABC scores (Extended Data Fig. 6d,e). This indicates that *MYC* may be uniquely sensitive to enhancer–promoter rewiring. We reasoned that other genes might also show similar responsiveness or invariance to changes in ABC scores. To identify such genes, we computed correlation coefficients for all protein-coding genes between RNA expression and ABC scores across 30 cell lines for which we had Hi-C, H3K27ac ChIP–seq and RNA-seq data. The Pearson correlations showed a positive shift compared to randomly shuffled controls (Fig. 5b), indicating that some genes show a strong correlation between gene expression and ABC scores, such as the transcriptional factor *ISL1* (Fig. 5c, $R^2 = 0.91$). Inspection of chromatin interaction frequencies and H3K27ac near *ISL1* showed that both features varied between cells with low (MDA-MB–468) or high (SK-N-DZ) expression and ABC scores (Fig. 5d). Likewise, both 'Activity' and 'Contact' are globally correlated with gene expression (Extended Data Fig. 6f,g).

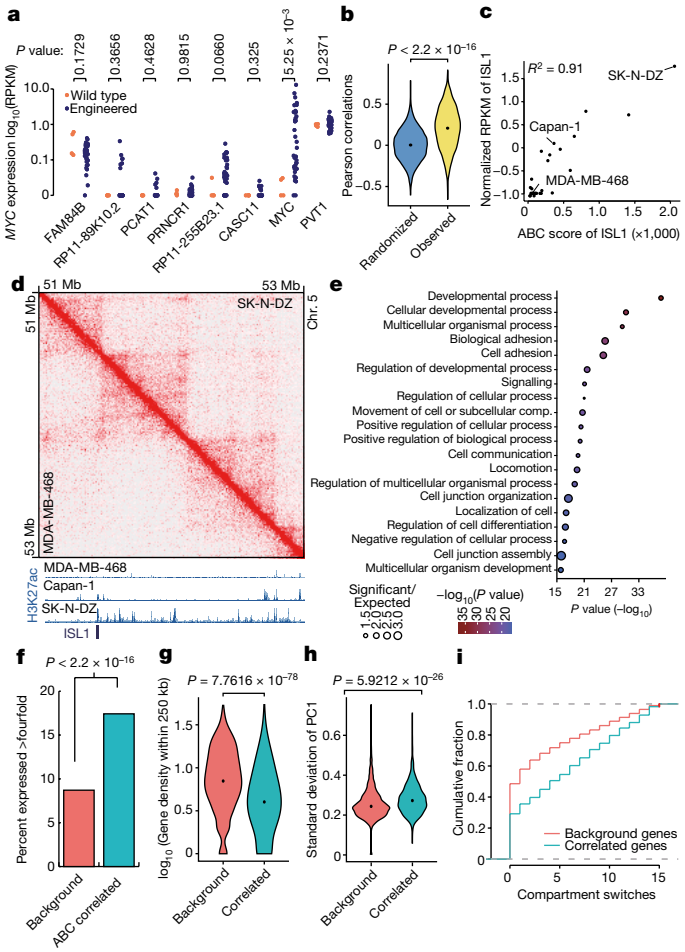

Fig. 5 | Genome-wide ABC models across cell lines. a, RNA-seq for all genes within the TAD at the *MYC* locus with evidence of expression in at least one clone. Expression is shown for wild-type clones (orange) and engineered clones (blue) (*P* value from a two-sided Wilcoxon rank sum test). **b**, Pearson correlations between RPKMs and ABC scores for all genes across 30 cancer cell lines compared with randomly shuffled controls. (*P* value from a two-sided Kruskal–Wallis test). **c**, RPKM and ABC scores for the gene *ISL1*. **d**, Hi-C contact frequency in SK-N-DZ (top right) and MDA-MB-468 (bottom left) near *ISL1*. H3K27ac ChIP–seq tracks of three cell lines with different expression levels of *ISL1* are shown below. **e**, GO analysis of 962 genes with significant correlations (FDR 1%) between RPKMs and ABC score. FDR is calculated empirically by randomly shuffling the ABC scores 1,000 times. "Component" is abbreviated "comp". **f**, Percentage of ABC-correlated or background genes upregulated more than fourfold relative to the mean expression when in the same TAD as a SV from the PCAWG dataset (*P* value from a Fisher's exact test). **g**, Gene density within 250 kb of the 962 correlated and non-correlated genes (*P* value from a two-sided Kruskal–Wallis test). **h**, Standard deviation of PC1 in the group of 962 correlated genes and the group of the rest of genes (*P* value from a two-sided Kruskal–Wallis test). **i**, Empirical cumulative density-function curves of the number of compartment switches for correlated and background genes. Genes are assigned a compartment type (A or B) based on the sign of their compartment score (A, positive; B, negative). The number of compartment switches is calculated as the number of cell lines that show an A or B compartment type that is different from the majority compartment type for that gene.

To identify sets of genes with significant correlation between ABC score and gene expression, we randomly shuffled ABC scores to calculate empirical FDRs. We found 962 genes with a significant correlation between ABC score and gene expression at an FDR 1% threshold (Pearson correlation = 0.5563, Supplementary Table 5). By using ABC scores to predict enhancer–gene linkages, we observed that ABC-correlated genes engage in slightly more enhancer–gene connections than non-correlated genes (Extended Data Fig. 6h, 1.86 enhancers/gene versus 1.79 enhancers/gene, $P = 6 \times 10^{-5}$, paired Wilcoxon test). However, ABC-correlated genes engaged only 3.9% more enhancers per gene. This suggests that association with enhancers is insufficient to distinguish ABC-correlated and non-correlated genes. Instead, ABC-correlated genes may be more 'responsive' to changes in their local enhancer landscape.

To determine features that distinguish ABC-responsive genes, we performed gene ontology (GO) analysis and identified terms related to cellular development, differentiation, migration and communication (Fig. 5e), suggesting that ABC-correlated genes may represent specific classes of developmentally regulated genes. Consistent with their potential roles in developmental regulation, ABC-responsive genes were over-represented for transcription factors (Extended Data Fig. 6i)[58]. ABC-responsive genes are also more likely to be classified as 'oncogenes' according to the Cosmic cancer gene census (Extended Data Fig. 6j). Furthermore, by using gene expression and SV data from the PCAWG dataset, we observe that ABC-correlated genes are more likely to be upregulated when in the same TAD as a SV compared with non-ABC-correlated genes (Fig. 5f), consistent with these genes being more sensitive to changes in their local enhancer landscape. In addition, ABC-correlated genes are in more gene-poor regions of the genome (Fig. 5g) and are more likely to switch A or B compartments between cell types (Fig. 5h,i), suggesting that such genes may have distinct modes of regulation. Taken together, these results revealed distinct sets of genes in the genome that show marked correlations with ABC scores, particularly developmentally regulated genes. Understanding the mechanistic basis for this distinction will be important for future studies.

Discussion

Somatic rearrangements that alter the gene regulatory landscape have long been recognized as potential cancer driver mutations[59]. However, as with many 'non-coding' somatic mutations, evaluating the functional consequences of any specific event is challenging[60]. Previous studies of the impact of SVs on 3D genome structure and gene expression have shown highly variable effects, from substantial differences in expression and phenotypic alterations[61] to minimal differences in gene expression[4,5]. This has led to confusion over what role SVs and alterations to 3D genome structure more generally play in gene regulation.

To address these issues, we have examined SVs in cell lines and patient samples and have identified numerous loci showing evidence of recurrent alterations in 3D genome structure across cancer samples. Despite evidence for recurrence, such sites still show highly variable gene expression patterns. By using CRISPR–Cas9 genome editing to generate engineered SVs, we find that heterogeneity in expression can be primarily explained by enhancer activity and 3D genome structure of the partner region. Furthermore, predictive models that integrate chromatin contacts and enhancer activity, such as ABC models, can predict the likelihood of *MYC* activation. These results may help explain the differences in the impact of structural variation on gene expression observed in previous studies and help point a path forward to using predictive models to interpret the effects of SVs in cancer patient samples. In particular, we suggest that ABC models have important implications for understanding the impact of non-coding somatic mutations. In the future, such models may be used to determine whether a specific genetic event is an oncogenic driver in patient tumour samples.

There are several interesting implications of our engineered rearrangements and ABC models on the role of super-enhancers in long-range gene regulation. First, we observed that loci with TAD fusion events are more likely to contain super-enhancers, yet in our engineered rearrangements, the presence of a super-enhancer does not lead to a uniform or consistent change in *MYC* expression. However, in the context of ABC models, super-enhancers will still play an outsized

role. Specifically, contact frequency measured by Hi-C has been shown to decay exponentially as the linear genomic distance between loci increases[62], whereas super-enhancer elements display exponentially stronger signals than typical enhancers[63]. When considered as the product of these two forces in ABC models, super-enhancers are probably the only stand-alone regulatory elements capable of generating strong activating signals at large (more than 300 kb) genomic distances (Extended Data Fig. 6k–m). The use of ABC models also does not require super-enhancers to be considered as a separate class of regulatory elements distinct from typical enhancers. Instead, what distinguishes super-enhancers, and would contribute to their having an outsized role in long-range gene regulation, is the fact that they display exponentially stronger activity signals than 'typical' enhancers.

Finally, we suggest that the predictive power of ABC models is also potentially suggestive of mechanism. In our ABC models, the expression of a gene is related to the sum of the enhancers it contacts weighted by the strength of those contacts. This suggests that genes may 'sample' distal enhancers through long-range chromatin contacts and integrate these interactions into final gene expression levels. Such 'sampling' probably occurs through mechanisms such as loop extrusion. For a given gene, whether this integration is linear or nonlinear, which has been recently suggested in a study examining the effects of a single enhancer–gene pair[64], is an important issue for future studies. Furthermore, our results also indicate that ABC models are generally predictive of gene expression, but only for a subset of genes. We would note that previous work describing ABC models for predicting enhancer–gene connections found that these models are best suited to predicting enhancer–gene connections of tissue-specific genes[56]. This suggests that such mechanisms of distal enhancer integration may only apply to specific sets or types of genes, such as developmental or tissue-specific genes, although the mechanistic basis for this distinction remains unclear. Moving forward, it will be critical to determine whether such ABC-responsive genes are also like *MYC* in their susceptibility to enhancer–promoter rewiring, and to further define the features that contribute to this susceptibility. This information will be critical to developing models that predict how somatic structural rearrangements affect oncogene expression.

Online content

Any methods, additional references, Nature Portfolio reporting summaries, source data, extended data, supplementary information, acknowledgements, peer review information; details of author contributions and competing interests; and statements of data and code availability are available at https://doi.org/10.1038/s41586-022-05504-4.

1. Dekker, J. & Mirny, L. The 3D genome as moderator of chromosomal communication. *Cell* **164**, 1110–1121 (2016).
2. Yu, M. & Ren, B. The three-dimensional organization of mammalian genomes. *Annu. Rev. Cell Dev. Biol.* **33**, 265–289 (2017).
3. Spielmann, M., Lupianez, D. G. & Mundlos, S. Structural variation in the 3D genome. *Nat. Rev. Genet.* **19**, 453–467 (2018).
4. Ghavi-Helm, Y. et al. Highly rearranged chromosomes reveal uncoupling between genome topology and gene expression. *Nat. Genet.* **51**, 1272–1282 (2019).
5. Akdemir, K. C. et al. Disruption of chromatin folding domains by somatic genomic rearrangements in human cancer. *Nat. Genet.* **52**, 294–305 (2020).
6. Levine, M., Cattoglio, C. & Tjian, R. Looping back to leap forward: transcription enters a new era. *Cell* **157**, 13–25 (2014).
7. Leder, P. et al. Translocations among antibody genes in human cancer. *Science* **222**, 765–771 (1983).
8. Taub, R. et al. Translocation of the c-myc gene into the immunoglobulin heavy chain locus in human Burkitt lymphoma and murine plasmacytoma cells. *Proc. Natl Acad. Sci. USA* **79**, 7837–7841 (1982).
9. Weischenfeldt, J. et al. Pan-cancer analysis of somatic copy-number alterations implicates IRS4 and IGF2 in enhancer hijacking. *Nat. Genet.* **49**, 65–74 (2017).
10. Northcott, P. A. et al. Enhancer hijacking activates GFI1 family oncogenes in medulloblastoma. *Nature* **511**, 428–434 (2014).
11. Peifer, M. et al. Telomerase activation by genomic rearrangements in high-risk neuroblastoma. *Nature* **526**, 700–704 (2015).
12. Groschel, S. et al. A single oncogenic enhancer rearrangement causes concomitant EVI1 and GATA2 deregulation in leukemia. *Cell* **157**, 369–381 (2014).
13. Hnisz, D. et al. Activation of proto-oncogenes by disruption of chromosome neighborhoods. *Science* **351**, 1454–1458 (2016).
14. Wang, X. et al. Genome-wide detection of enhancer-hijacking events from chromatin interaction data in rearranged genomes. *Nat. Methods* **18**, 661–668 (2021).
15. Flavahan, W. A. et al. Insulator dysfunction and oncogene activation in IDH mutant gliomas. *Nature* **529**, 110–114 (2016).
16. Flavahan, W. A. et al. Altered chromosomal topology drives oncogenic programs in SDH-deficient GISTs. *Nature* **575**, 229–233 (2019).
17. Dixon, J. R. et al. Integrative detection and analysis of structural variation in cancer genomes. *Nat. Genet.* **50**, 1388–1398 (2018).
18. Barutcu, A. R. et al. RUNX1 contributes to higher-order chromatin organization and gene regulation in breast cancer cells. *Biochim. Biophys. Acta* **1859**, 1389–1397 (2016).
19. Harewood, L. et al. Hi-C as a tool for precise detection and characterisation of chromosomal rearrangements and copy number variation in human tumours. *Genome Biol.* **18**, 125 (2017).
20. Rao, S. S. et al. A 3D map of the human genome at kilobase resolution reveals principles of chromatin looping. *Cell* **159**, 1665–1680 (2014).
21. Wang, Z. et al. The properties of genome conformation and spatial gene interaction and regulation networks of normal and malignant human cell types. *PLoS One* **8**, e58793 (2013).
22. Taberlay, P. C. et al. Three-dimensional disorganization of the cancer genome occurs coincident with long-range genetic and epigenetic alterations. *Genome Res.* **26**, 719–731 (2016).
23. Guo, Y. et al. CRISPR inversion of CTCF sites alters genome topology and enhancer/promoter function. *Cell* **162**, 900–910 (2015).
24. Akdemir, K. C. et al. Somatic mutation distributions in cancer genomes vary with three-dimensional chromatin structure. *Nat. Genet.* **52**, 1178–1188 (2020).
25. Consortium, E. P. An integrated encyclopedia of DNA elements in the human genome. *Nature* **489**, 57–74 (2012).
26. Burton, J. N. et al. Chromosome-scale scaffolding of de novo genome assemblies based on chromatin interactions. *Nat. Biotechnol.* **31**, 1119–1125 (2013).
27. Engreitz, J. M., Agarwala, V. & Mirny, L. A. Three-dimensional genome architecture influences partner selection for chromosomal translocations in human disease. *PLoS One* **7**, e44196 (2012).
28. Naumova, N. et al. Organization of the mitotic chromosome. *Science* **342**, 948–953 (2013).
29. Seaman, L. et al. Nucleome analysis reveals structure-function relationships for colon cancer. *Mol. Cancer Res.* **15**, 821–830 (2017).
30. Marcotte, R. et al. Functional genomic landscape of human breast cancer drivers, vulnerabilities, and resistance. *Cell* **164**, 293–309 (2016).
31. Ngoc, P. C. T. et al. Identification of novel lncRNAs regulated by the TAL1 complex in T-cell acute lymphoblastic leukemia. *Leukemia* **32**, 2138–2151 (2018).
32. Harenza, J. L. et al. Transcriptomic profiling of 39 commonly-used neuroblastoma cell lines. *Sci. Data* **4**, 170033 (2017).
33. Korbel, J. O. & Campbell, P. J. Criteria for inference of chromothripsis in cancer genomes. *Cell* **152**, 1226–1236 (2013).
34. Baca, S. C. et al. Punctuated evolution of prostate cancer genomes. *Cell* **153**, 666–677 (2013).
35. Cortes-Ciriano, I. et al. Comprehensive analysis of chromothripsis in 2,658 human cancers using whole-genome sequencing. *Nat. Genet.* **52**, 331–341 (2020).
36. Stephens, P. J. et al. Massive genomic rearrangement acquired in a single catastrophic event during cancer development. *Cell* **144**, 27–40 (2011).
37. Forcato, M. et al. Comparison of computational methods for Hi-C data analysis. *Nat. Methods* **14**, 679–685 (2017).
38. Davidson, I. F. & Peters, J. M. Genome folding through loop extrusion by SMC complexes. *Nat. Rev. Mol. Cell Biol.* **22**, 445–464 (2021).
39. Veloza, L., Ribera-Cortada, I. & Campo, E. Mantle cell lymphoma pathology update in the 2016 WHO classification. *Ann. Lymphoma* **3**, 2616–2695 (2019).
40. Canela, A. et al. Genome organization drives chromosome fragility. *Cell* **170**, 507–521 e518 (2017).
41. Dixon, J. R. et al. Topological domains in mammalian genomes identified by analysis of chromatin interactions. *Nature* **485**, 376–380 (2012).
42. Nora, E. P. et al. Spatial partitioning of the regulatory landscape of the X-inactivation centre. *Nature* **485**, 381–385 (2012).
43. Zhang, Y. et al. Transcriptionally active HERV-H retrotransposons demarcate topologically associating domains in human pluripotent stem cells. *Nat. Genet.* **51**, 1380–1388 (2019).
44. Dixon, J. R. et al. Chromatin architecture reorganization during stem cell differentiation. *Nature* **518**, 331–336 (2015).
45. Schuijers, J. et al. Transcriptional dysregulation of MYC reveals common enhancer-docking mechanism. *Cell Rep.* **23**, 349–360 (2018).
46. Shi, J. et al. Role of SWI/SNF in acute leukemia maintenance and enhancer-mediated Myc regulation. *Genes Dev.* **27**, 2648–2662 (2013).
47. Fulco, C. P. et al. Systematic mapping of functional enhancer-promoter connections with CRISPR interference. *Science* **354**, 769–773 (2016).
48. Beroukhim, R. et al. The landscape of somatic copy-number alteration across human cancers. *Nature* **463**, 899–905 (2010).
49. Delgado, M. D. & Leon, J. Myc roles in hematopoiesis and leukemia. *Genes Cancer* **1**, 605–616 (2010).
50. Li, Y. et al. Patterns of somatic structural variation in human cancer genomes. *Nature* **578**, 112–121 (2020).
51. Zhang, Y. et al. Spatial organization of the mouse genome and its role in recurrent chromosomal translocations. *Cell* **148**, 908–921 (2012).
52. Arber, D. A. et al. The 2016 revision to the World Health Organization classification of myeloid neoplasms and acute leukemia. *Blood* **127**, 2391–2405 (2016).
53. Doyle, L. A. Sarcoma classification: an update based on the 2013 World Health Organization classification of tumors of soft tissue and bone. *Cancer* **120**, 1763–1774 (2014).

54. Cong, L. et al. Multiplex genome engineering using CRISPR/Cas systems. *Science* **339**, 819–823 (2013).
55. Zimmerman, M. W. et al. MYC drives a subset of high-risk pediatric neuroblastomas and is activated through mechanisms including enhancer hijacking and focal enhancer amplification. *Cancer Discov.* **8**, 320–335 (2018).
56. Fulco, C. P. et al. Activity-by-contact model of enhancer-promoter regulation from thousands of CRISPR perturbations. *Nat. Genet.* **51**, 1664–1669 (2019).
57. Zhou, J. Sequence-based modeling of three-dimensional genome architecture from kilobase to chromosome scale. *Nat. Genet.* **54**, 725–734 (2022).
58. Lambert, S. A. et al. The human transcription factors. *Cell* **172**, 650–665 (2018).
59. Bradner, J. E., Hnisz, D. & Young, R. A. Transcriptional addiction in cancer. *Cell* **168**, 629–643 (2017).
60. Khurana, E. et al. Role of non-coding sequence variants in cancer. *Nat. Rev. Genet.* **17**, 93–108 (2016).
61. Lupianez, D. G. et al. Disruptions of topological chromatin domains cause pathogenic rewiring of gene-enhancer interactions. *Cell* **161**, 1012–1025 (2015).
62. Lieberman-Aiden, E. et al. Comprehensive mapping of long-range interactions reveals folding principles of the human genome. *Science* **326**, 289–293 (2009).
63. Whyte, W. A. et al. Master transcription factors and mediator establish super-enhancers at key cell identity genes. *Cell* **153**, 307–319 (2013).
64. Zuin, J. et al. Nonlinear control of transcription through enhancer-promoter interactions. *Nature* **604**, 571–577 (2022).

Methods

Cell culture and patient tumour samples

A detailed list of cell lines used as part of this study is in tabular form in Supplementary Table 1 and is also detailed here. Cells were routinely tested for *Mycoplasma* by using the Universal Mycoplasma Detection Kit (ATCC 30-1012K) and all tested negative. In addition, all cell lines not directly obtained from a repository were subject to STR profiling (ATCC) to confirm the correct cellular identity.

The following cell lines were cultured in Dulbecco's Modified Eagle Medium (Mediatech 10-013-CV) supplemented with 10% fetal bovine serum (Sigma F0926-500ML) and 100 units ml^{-1} of penicillin–streptomycin (Life Technologies 15140122): MDA-MB-468, MDA-MD-231, MDA-MB-436, Caov-3, SW-626, SK-OV-3, A2058, A172, SW-1088, U-118-MG and U343. The following cell lines were cultured in Eagle's Minimal Essential Medium (Quality Biological 112-018-101) supplemented with 10% fetal bovine serum (Sigma F0926-500ML) and 100 units ml^{-1} of penicillin–streptomycin (Life Technologies 15140122): HS-578-T, BT-20, U-87-MG, MG-63, DU-145 and SK-N-SH.

The following cell lines were cultured in RPMI-1640 medium (Lonza 12-167F) supplemented with 10% fetal bovine serum (Sigma F0926-500ML) and 100 units ml^{-1} of penicillin–streptomycin (Life Technologies 15140122): DU4475, HCC1187, HCC1599, HCC1806, HCC1937, HCC2218, HCC38, HCC70, HCC1569, HCC2157, BT-549, MOLM-13, MV4;11, ML-2, Jeko-1, Granta, Rec-1, Maver-1, Mino, CESS, Jurkat, NCI-H596, NCI-H1437, NCI-H1563, NCI-H1573 and NCI-H1975. The following cell lines were cultured in RPMI-1640 medium (Lonza 12-167F) supplemented with 15% fetal bovine serum (Sigma F0926-500ML), 100 units ml^{-1} of penicillin–streptomycin (Life Technologies 15140122) and 2 mM L-glutamine: MOLT-4, RPMI-8402 and CCRF-CEM.

SK-N-DZ cells were cultured in Dulbecco's Modified Eagle Medium (Mediatech 10-013-CV) supplemented with 10% fetal bovine serum (Sigma F0926-500ML), 100 units ml^{-1} of penicillin–streptomycin (Life Technologies 15140122) and 1× non-essential amino acids (Life Technologies 11140050). TT cells were cultured in Ham's F-12K medium (ThermoFisher 21127022) supplemented with 10% fetal bovine serum (Sigma F0926-500ML) and 100 units ml^{-1} of penicillin–streptomycin (Life Technologies 15140122). Capan-1 and HL-60 cell lines were cultured in Iscove's Modified Dulbecco's Medium (ThermoFisher 12440053) supplemented with 10% fetal bovine serum (Sigma F0926-500ML) and 100 units ml^{-1} of penicillin–streptomycin (Life Technologies 15140122).

The following cell lines were obtained from ATCC: HCC1569 (CRL-2330), MDA-MB-436 (HTB-130), DU4475 (HTB-123), HCC1187 (CRL-2322), HCC1599 (CRL-2331), HCC1937 (CRL-2336), HCC2218 (CRL-2343), HCC38 (CRL-2314), HCC70 (CRL-2315), MDA-MB-468 (HTB-132), HCC2157 (CRL-2340), BT-549 (HTB-122), HS-578-T (HTB-126), BT-20 (HTB-19), HCC1806 (CRL-2335), Caov-3 (HTB-75), SW-626 (HTB-78), SK-OV-3 (HTB-77), A172 (CRL-1620), SW-1088 (HTB-12), U-118 MG (HTB-15), U-87 MG (HTB-14), HL-60 (CCL-240), CESS (TIB-190), NCI-H596 (HTB-178), NCI-H1437 (CRL-5872), NCI-H1563 (CRL-5875), NCI-H1573 (CRL-5877), NCI-H1975 (CRL-5908), SK-N-SH (HTB-11) and SK-N-DZ (CRL-2149). Of note, the U-118-MG cell line is known to share genetic origin with a separate glioma cell line U138-MG. This cell line was purchased directly from ATCC as part of their glioma cell line panel (TCP-1018). Given that both of these cell lines represent gliomas, that it is included to be representative for pan-cancer profiling and that we only include the U-118-MG cell line, we felt that its inclusion was justified despite its shared origin.

The following cell lines were obtained from Coriell: RPMI-8402 (GM03639), MOLT-4 (GM02219) and CCRF-CEM (GM03671). The following cell lines were a gift from the laboratory of A. Deshpande: MOLM-13, MV4;11, ML-2, Jeko-1, Granta, Rec-1, Maver-1 and Mino. The following cell lines were a gift from the laboratory of A. Saghatelian: A2058, Capan-1, U343, MG-63, DU-145 and TT. Jurkat cells were a gift from the laboratory of B. Lillemeier.

Biospecimens were collected by the Moores Cancer Center Biorepository and Tissue Technology shared resource from consented patients under a University of California, San Diego Human Research Protections Program Institutional Review Board approved protocol (HRPP no. 090401). Samples were flash frozen in liquid nitrogen. All research involving human tumour specimens was also reviewed by the Institutional Review Board at the Salk Institute.

Sequencing library generation

Hi-C was performed by using the in situ method as previously described[20]. In summary, for assays using cell lines, adherent cells were fixed for 10 min at room temperature by using 1% formaldehyde. For suspension cells, this was done after resuspending cells in fresh media at a concentration of 1×10^6 cells per ml. Cells were quenched with 0.2 M glycine, pelleted and washed twice with 1× Dulbecco's phosphate-buffered saline (DPBS). Cells were incubated in ice-cold lysis buffer (10 mM Tris–HCl pH 8.0, 10 mM NaCl, 0.2% Igepal) for 15 min on ice and washed twice with 1× NEB Buffer 2. The digestion and further processing of the samples is described below (see paragraph following processing for patient tumour samples).

For patient tumour samples, the tumour was removed from liquid nitrogen storage and weighed when still frozen. By using a mortar and pestle on a bed of dry ice, the samples were pulverized when frozen until they formed a fine powder. The pulverized tissue was transferred to a 15 ml tube containing 10 ml of 1× DPBS and fixed by using 2% formaldehyde for 10 min. The samples were quenched with 0.2 M glycine for 5 min. The tissue was washed twice in 1× DPBS. After removing the supernatant, the pellets were frozen at −80 °C until further processing. When ready for Hi-C experiments, the pellets were thawed and resuspended in 3 ml of tissue lysis buffer (10 mM Tris–HCl pH 8.0, 5 mM $CaCl_2$, 3 mM MgAc, 2 mM EDTA, 0.2 mM EGTA, 1 mM dithiothreitol, 0.1 mM phenylmethyl sulfonyl fluoride and 1× complete protease inhibitors). The samples were transferred to an M-tube and run through the Protein M-tube program on a gentleMACs tissue dissociator (Miltenyi). After the dissociation, an additional 3 ml of tissue lysis buffer with 0.4% Triton X-100 was added to the sample and the solution was passed through a 40 μM strainer. The tube and cell strainer were washed with an additional 2 ml of 0.2% tissue lysis buffer with 0.2% Triton X-100. The sample was centrifuged and washed with an additional 1 ml of tissue lysis buffer with 0.2% Triton X-100.

For both cell line and tissue samples processed as described above, the digestion and Hi-C library preparation proceeded similarly based on the in situ Hi-C protocol[20]. The pellet was resuspended in 50 μl of 0.5% SDS and incubated for 10 min at 62 °C. Then 145 μl of water and 25 μl of 10% Triton X-100 were added to quench the SDS for 15 min at 37 °C. Next 25 μl of 10× NEB Buffer 2 was added to the samples. Cells were digested with 500 U of MboI restriction enzyme (NEB) in NEB Buffer 2. DNA ends were filled in with deoxynucleotide triphosphates (dNTPs), including biotin-14-dATP (Jena), by using Klenow polymerase (NEB). Chromatin ends were ligated by using T4 DNA ligase. DNA was then purified and sheared on a Covaris M-series ultrasonicator. Biotinylated fragments were purified by using the My T1 Streptavidin coated beads (Life Technologies) and subject to on-bead library preparation as described previously[20]. Libraries were sequenced by using the Illumina NextSeq 500 as paired-end 42 bp reads.

RNA-seq was performed by first harvesting cells in Trizol (Life Technologies) according to the manufacturer's instructions. RNA was then isolated by using the Purelink RNA Mini Kit (Life Technologies) with Purelink on-column DNase I treatment. Stranded messenger RNA-seq libraries were generated from 1–2 μg of RNA by using the Illumina Stranded mRNA kit according to the manufacturer's recommendation. Libraries were pooled and sequenced on NextSeq 500 by using paired-end 42 bp reads.

CRISPR–Cas9 translocation engineering

Genome engineering was performed by expressing gRNA and Cas9 containing plasmids in SK-N-DZ cells. In our test set of experiments, we used two plasmids per experiment, one to express guides in proximity to *MYC* on chromosome 8 and a second to express guides of the putative partner regions. In our validation set of experiments, dual guides were cloned into a single vector. All guides were synthesized by Integrated DNA Technologies (IDT). Cloning of the guides was carried out as previously described[65]. In our two-plasmid system, all chromosome 8 guides were cloned into the pX458 plasmid (expressing green fluorescent protein (GFP), Addgene no. 48138, a gift from F. Zhang), and the partner region guides were cloned into a modified version of pX458 in which the GFP was replaced by mCherry (a gift from A. Kim). We designed three to four guides per locus. These were transfected as pairs, with one guide targeting chromosome 8 and one guide targeting the partner region, for a total of 12 guide pairs (3 × 4) per locus. In our single-plasmid system, the two guides were cloned into the pX458-mCherry plasmid. Transfection was carried by electroporation of 1 μg of each plasmid by using the Lonza 4D Nucleofection SF kit into 200,000–500,000 SK-N-DZ cells per transfection. We used the DS-150 program for electroporation. Cells were allowed to recover for 10 min and were then plated in fresh media. After two days, cells expressing both chromosome 8 and partner region guides were isolated. Sorted cells were allowed to recover for one to two weeks before plating manually as single cells in 96-well plates. SK-N-DZ cells typically grow as colonies, such that after two weeks, we visually inspected the 96-well plates and excluded wells containing more than one colony.

To screen for engineered clones, we designed PCR primers that flanked the gRNA target sequences in the genome. Specifically, one primer was centromeric to the guides on chromosome 8, whereas the second guide was telomeric to the guides on the putative partner region. Cells in 96-well plates were split into replicate plates. One plate was then harvested by using 20 μl of QuickExtract (Lucigen) per well. The samples were incubated in a 96-well T100 thermal cycler (Bio-Rad) by using the following programme: 65 °C for 15 min, 68 °C for 15 min and 98 °C for 10 min. The samples were diluted by adding 30 μl of water. PCR was then performed by using Taq polymerase (Life Technologies) in 20 μl volumes by using 5 μl of QuickExtract DNA per reaction. The PCR products were resolved on 96-well E-gels (Life Technologies). Wells with positive PCR products were propagated on the replicate 96-well plate and all other wells were discarded.

Once a given clone reached sufficient density, we obtained purified genomic DNA by using the Qiagen Blood & Tissue DNA Isolation Kit (Qiagen). PCR was repeated by using 50 ng of DNA. If this confirmatory PCR was also positive, the PCR product was excised from the gel by using the Qiagen Gel Extraction kit and subject to Sanger Sequencing (Eton). Only clones with unique breakpoint junctions from Sanger sequencing were further processed to ensure that each clone was distinct and not the product of propagating the daughter cells of the same original rearrangement. Finally, the large-scale rearrangement was validated by chromosome painting by using commercially available probes according to the manufacturer's instructions (Cytocell). If the cells were ultimately positive for the engineered rearrangement by PCR, Sanger sequencing and chromosome painting, we harvested cells for Hi-C and RNA-seq and generated sequencing libraries for each clone.

mClover2 reporter engineering

We engineered SK-N-DZ cells containing a mClover2 reporter integrated into the 3′ UTR of the *MYC* gene. To generate the donor plasmid for the mClover2 reporter knock-in, we first PCR amplified approximately 3 kb fragment near the *MYC* stop codon (including approximately 1.5 kb both upstream and downstream) and cloned it into a pCR-Blunt II-TOPO vector (Invitrogen). We then inserted a T2A-mClover2 tag (PCR amplified from dClover2-N1, Addgene no. 54538, a gift from M. Davidson) to the 3′ end of MYC, followed by a loxP-PGK-Neo^{R}-loxP fragment (PCR amplified from Oct4-ires-EGFP, Addgene no. 21547, a gift from R. Jaenisch). gRNAs were designed near the *MYC* stop codon and cloned into pX458 with mCherry. After linearization of the donor plasmid, the donor plasmid and gRNA plasmid (500 ng each) were co-transfected into 1 million SK-N-DZ cells by using the Lonza 4D Nucleofection SF kit. After 48 h, transfected cells were transferred to a 10 cm plate and treated with 1 mg ml^{-1} of Geneticin (Gibco) for five days. By the end of Geneticin treatment, half of the cells were harvested for gDNA extraction, followed by a bulk cell PCR testing (by using one primer upstream of the *MYC* stop codon and another inside the insertion) to examine if there was successful integration. Cells were then plated manually as single cells in 96-well plates. After two weeks, we visually inspected the 96-well plates and excluded wells containing more than one colony. By using the same PCR primers for bulk PCR testing, we screened for engineered clones in the same way described above.

Enhancer deletion experiment

By using the SK-N-DZ cells with the *MYC*-mClover2 reporter, we generated a chromosome 1 to chromosome 8 translocation by using CRISPR–Cas9 engineering with the same gRNAs used to generate chr. 1 clone #1. mClover2+ cells were sorted into 96-well plates by using FACS. Clones were screened by using the same primers used for chr. 1 clone #1 to identify clones harbouring the t(1;8) translocation. We isolated multiple clonal cell lines and performed flow cell cytometry to verify mClover2 expression, RNA-seq to verify if the expression of *MYC* is consistent with chr. 1 clone #1 and #2 and Hi-C to demonstrate the presence of the translocated allele.

In the clone with a chromosome t(1;8) translocation, we performed additional CRISPR–Cas9 engineering to delete the genomic enhancer at chr. 1:49,045,908–49,063,390, which contains the strongest H3K27ac peak near the translocated chr. 1 breakpoint. Bulk cell mClover2 expression level was compared between cells transfected with guides deleting the enhancer and control guides that do not introduce any deletion. We defined the 'mClover2 low' population of cells as cells with mClover2 expression greater than one standard deviation below the mean of the mClover2 expression level in cells transfected with control gRNAs.

To examine clonal RNA-seq expression levels from cells with the deleted enhancer, we plated cells after introducing the deletion gRNAs as single cells in 96-well plates. PCR tests were used to screen for multiple cell lines with deletions. We then determined whether the deletions were on the same allele as the translocation or the non-translocated allele. To accomplish this, we first had to determine which polymorphisms could distinguish the translocated and non-translocated alleles. We started by calling variants from Hi-C sequencing reads by using GATK Haplotype caller, including steps of indel realignment and base recalibration[66]. We then filtered only single-nucleotide polymorphisms (SNPs) with a quality of 'PASS' for further processing. We performed haplotype phasing by using the Hi-C data as previously described[67] by using Hapcut 2 (ref. [68]). This generates chromosome length haplotypes that facilitate distinguishing each chromosome into one of two haplotypes, A or B. We examined Hi-C reads within 1 Mb of the chr. 1/chr. 8 translocation breakpoint to determine which haplotypes were involved in the translocation. We observed that all breakpoint proximal reads supported haplotype B on chromosome 8 being translocated to haplotype A on chromosome 1 (n = 332 reads for chr. 8 haplotype assignment, n = 118 for chr. 1). This unambiguously establishes that the haplotypes involved in the engineered translocation. We identified three SNPs (rs17105425, rs12410172 and rs11581331) within the chr. 1:49,045,908–49,063,390 enhancer that allowed us to distinguish whether the wild-type or translocated haplotype carried the deletion. To achieve this, we used Sanger sequencing across these polymorphisms in the deleted clones to determine which haplotype the deletion occurred. We then performed RNA-seq for all enhancer deletion engineered clones and compared the *MYC* expression between

the group with deletion on translocated allele with that on wild-type allele as a control.

RNA-seq analysis

RNA-seq data were aligned by using STAR[69] to the hg38 reference genome. PCR duplicates were removed, and read counts were quantified over GENCODE genes (v.25) by using HTSeq[70] and subject to RPKM normalization. Fusion genes were identified by using STAR-fusion[71]. We filtered the initial calls by using multiple criteria. First, we removed genes for which expression was less than 1 RPKM as predicted by STAR-fusion. Second, we merged all fusion genes for which each predicted break end was within 500 kb of another fusion gene from the same cell line. This reduces the number of sites at which multiple fusion genes may be called owing to alternative transcript isoforms occurring across a single breakpoint. In addition, this also ensures that when evaluating the sensitivity of Hi-C-based SV calls that we do not consider the same breakpoint more than once. Third, we removed fusion genes that showed recurrent fusions across the samples. None of the samples used for fusion gene analysis carried known high-frequency fusion genes (for example, from chronic myelogenous leukaemia samples), so this step filtered out a subset of fusion genes that appear to reflect mapping and alignment anomalies.

Hi-C data processing

Hi-C data were aligned to the hg38 reference genome by using BWA-MEM[72]. Reads were filtered (mapping quality "MAPQ" ≥ 30) and paired by using a previously described pipeline[17]. PCR duplicate reads were removed by using Picard. Contact matrices were generated and normalized by using the iterative correction method[73]. TADs were identified as previously described[41]. To generate the merged TAD call set, we identified boundaries between TADs in five cell lines: hESCs, HCC38, MV411, DLD-1 and NCI-H1437. These boundaries were merged (enabling a padding of 40 kb) and unique boundaries were retained. The intervals between boundaries were then considered as the list of domain calls. Domains over 5 Mb were excluded as they typically were the intervening regions near centromeres.

Hi-C SV analysis

To identify SVs in Hi-C data, we used our previously described hicbreakfinder method[17] with default parameters at 10 kb resolution.

For analysis of frequently rearranged chromosomes (related to Extended Data Fig. 2c–e), we developed a simple statistical model for the frequency of intrachromosomal rearrangements per chromosome. We tested whether a given chromosome in a cell line shows evidence of 'clustering' of SVs. The baseline assumption is that SVs should be distributed randomly throughout the genome according to the size of each chromosome. Therefore, to test for clustering of SVs on a given chromosome, we first computed the total number of observed intrachromosomal rearrangements across all chromosomes in each cell line. To generate the expected number of SVs for a given chromosome, we divide the total number of intrachromosomal SVs in a given cell line by the size of the genome, then multiply this rate by the size of the chromosome that is tested for evidence of clustering (expected value = (total intra-events) × (chromosome size/genome size). We then calculated the *P* value for the observed number of intrachromosomal rearrangements per chromosome for all chromosomes in each sample given this expected rate. The *P* value was computed by using a Poisson distribution. Chromosomes with evidence of clustering are then called based on Bonferroni-corrected *P* values.

TAD fusion calling

To identify TAD fusion events in Hi-C data, we developed a neural-network-based machine-learning classifier. For each cell line, we generated a normalized Hi-C matrix, and TADs were called as previously described[41] at the resolution of 40 kb. For training the classifier, we randomly selected 10,000 different bins genome-wide at the same 40 kb resolution. The 10,000 random bins were then divided into a training set at the size of 7,000 and a cross-validation set at the size of 3,000. For each bin, we designated the sample bin as a coordinate of x, and then generated a submatrix at a size of 50 × 50 from the whole-genome Hi-C matrix at a square window of $[x - 2{,}000{,}000] \times [x + 2{,}000{,}000]$. Each submatrix was converted into a one-dimensional vector of size 2,500, which served as the input layer for each sample. We used a fully connected feed forward neural network with one hidden layer with 50 nodes and an output layer with only one node. For training samples, the output nodes were set to zero if the central bin is inside a TAD, or to one if the central bin is outside a TAD (in a boundary region). Matlab scripts were executed to train the neural network with all training samples for 400 iterations, by using backpropagation algorithm with sigmoid function as the activation function. The training was performed for each cell line in order to account for sample specific differences in Hi-C data. The trained neural network was then used to predict the output of cross-validation samples. Cross-validation samples were predicted as inside a TAD if the output node value is less than 0.5 and outside a TAD if the value is greater than or equal to 0.5. Prediction results were compared with TAD annotation from the same cell line for all cross-validation samples to generate precision and FDRs.

For predicting TAD fusion events, the model was then applied to chromosome rearrangements that we identified from Hi-C. Local rearranged submatrices from fused chromosomes were generated with extension from breakpoint in both directions for two megabases. The input layer was generated in the same way while using the bin of breakpoint as the central bin. These data were then used as input for the same neural network. The predictions were made by using the same criteria described above.

Identification of recurrent TAD fusion events

To identify domains affected by recurrent TAD fusion events, we quantified the total number of TAD fusion events predicted for each domain by using the merged set of TADs. After quantifying the total number of events per domain, we estimated the *P* value of observing the given number of events in that domain by using a two-sided Poisson test, in which the expected value is related to the overall number of TAD fusion events per base pair in the genome and the size of the domain in question. In order to determine the FDR at different significance thresholds, we randomly permuted TAD fusion calls per domain and recalculated the observed significance after such random permutations.

Whole-genome sequencing SV analysis

Somatic rearrangements, somatic copy number alterations and normalized gene expression data generated by the ICGC/TCGA PCAWG Consortium are described by the lead paper of the PCAWG Consortium[74] and are available for download at https://dcc.icgc.org/releases/PCAWG.

We obtained the consensus SV calls and annotations of each variation (deletions, inversions, duplications and complex rearrangements), which can be found at Synapse (https://www.synapse.org/) with accession number syn7596712, normalized gene expression values were obtained from syn5553985 and somatic copy number calls were obtained from syn8042988. For whole-genome sequencing defined SVs generated from the ICGC patient data cohort[50], we first performed minor filtration on the data. Specifically, we counted the frequency of breakpoints throughout the genome in 100 bp bins. We removed any SVs for which breakpoints were found in 100 bp bins containing rearrangements in more than ten patient samples. This filtration eliminated 0.4% of all SVs in the original dataset. We then filtered for 'inter-TAD' SVs by identifying variants for which one end maps within one TAD and a second maps within another TAD.

Patient RNA-seq and survival data were downloaded from the ICGC Data Portal PCAWG repository. Survival analysis was performed by using the 'survival' package in the R statistical programming language.

The differences in survival according to TAD fusion events was estimated by using the two-sided likelihood test derived from a Cox proportional hazards model.

ChIP–seq data analysis and super-enhancer identification

ChIP–seq data were downloaded from publicly accessible datasets[13,25,75–93]. Details of accession numbers and chromatin marks are listed in Supplementary Table 1. ChIP–seq data were aligned to the hg38 genome by using BWA[72]. See Supplementary Table 1 for a list of all public ChIP–seq datasets and their accession numbers that were analysed as part of this study. Peaks were called by using MACS2 (ref. [94]). Enhancers were defined as distal (more than 2.5 kb) H3K27ac peaks. Super-enhancers were determined according to the Rank Ordering of Super Enhancers (ROSE) algorithm[63] by using H3K27ac peaks.

END-seq data analysis

End sequencing (END-seq) data in MCF7 cells from ref. [40] was downloaded from the GEO database (GEO accession GSE99194). We specifically used the 'no treatment' conditions. Reads were aligned to the hg38 genome. The number of END-seq reads per TAD based on MCF7 TAD calls was quantified. We also separated domains into those that contain super-enhancers and those that do not based on H3K27ac ChIP–seq data in MCF7 (ref. [81]). Super-enhancers were determined according to the ROSE algorithm[63].

ABC models

For ABC models, we calculated the interaction frequency between the *MYC* promoter and a 3 Mb window distal to the site of the engineered breakpoint over the partner region of the genome by using 40 kb bins. To ensure that ABC scores were not influenced by differences in sequencing depth, the Hi-C data were first normalized according to the total number of contacts. We used H3K27ac data from wild-type SK-N-DZ cells[90] as the activity metric over the partner region. Peaks were quantified and the total signal present in each peak was normalized by the sample read depth. The ABC score was then calculated for each engineered clone by summing the enhancer activity multiplied by the promoter–enhancer interaction frequency. A similar strategy was used when calculating the aggregate enhancer activity, except this sum was not weighted by the interaction frequency.

For prediction of *MYC* expression, partner regions were classified as 'activating' or 'non-activating' by comparing expression of all replicate clones from a single partner site with the parental SK-N-DZ cells by using edgeR (FDR 5%). The activating and non-activating labels were then predicted by using different models. ROC curves were calculated by using the PRROC package in R.

Predicted contact maps resulting from SVs

To predict the consequence of SVs on 3D genome contact maps in silico, we used the Orca deep-learning tool[57]. We used the pretrained models derived from H1 hESCs (H1) and human foreskin fibroblasts for these predictions. The coordinates and strand of the breakpoints were derived from the base-pair-resolved SV breakpoints identified in Sanger sequencing analysis of the engineered rearrangements. The Orca tool generates predictions of contact frequency at different resolutions for different genomic windows surrounding the breakpoint site. We used the 4 Mb window with 16 kb bin size-based predictions as input for our Orca predicted ABC models. Orca outputs a log-transformed, distance normalized interaction matrix and a distance-expectation interaction matrix. From these we inferred a non-distance normalized interaction matrix by exponentiating the log-transformed prediction and multiplying it by the distance expectation for each bin.

Genome-wide gene expression correlation by using ABC models

The Hi-C data were first normalized according to the total number of contacts. For every protein-coding gene, we calculated the interaction frequency between the promoter and a 3 Mb window locally. In addition, if there is a translocation within 3 Mb of the transcription start site, interactions over the partner region within 3 Mb distance were also considered. We applied this procedure on 30 cell lines with published H3K27ac data as the activity metric over the same region. Peaks were quantified and the total signal present in each peak was normalized by the sample read depth. The ABC score was then calculated for each protein-coding gene in each cell line by summing the enhancer activity multiplied by the promoter–enhancer interaction frequency.

The Pearson correlation between the gene expression RPKMs and ABC scores was calculated for each protein-coding gene. We randomly shuffled the ABC scores as a control, and the Pearson correlation coefficient of the randomized control was also calculated. We repeated the shuffling of ABC scores in each gene 1,000 times to estimate the average FDR at different values of Pearson correlation coefficient. We defined ABC-responsive genes by setting Pearson correlation coefficient with FDR cut-off at 1%.

For calculation of enhancer–gene linkages by using ABC scores, we computed individual enhancer ABC scores for each gene and divided them by the total ABC score for each gene. We considered enhancer–gene connections with such enhancer–gene fractional ABC scores ≥0.1 based on previously described cut-offs for such enhancer–gene ABC scores[56]. GO analysis was applied to the ABC-responsive genes by using topGO[95]. The frequency of ABC-correlated or background genes classified as 'transcription factors' was determined by using annotations of previously published human transcription factors[58]. The frequency of ABC-correlated or background genes classified as oncogenes was evaluated by comparing the official gene names of each gene with genes classified as oncogenes according to the Cosmic cancer gene census. To compare ABC-correlated or background genes with expression changes in the PCAWG dataset, we first computed the fold-change relative to the average expression of each gene across all patient samples in the PCAWG dataset. We then calculated the fraction of ABC-correlated or background genes that showed greater than or equal to fourfold change relative to the average in the same TAD as a SV.

For compartment analysis, PC1 values at 100 kb resolution were calculated from Hi-C data of each cell line. We defined positive values as A compartment, negative values as B compartment and the number of compartment switches as the number of cell lines in the minority compartment in each 100 kb genomic bin. For each gene, the number of compartment switches of the genomic bin where the promoter is located was classified into ABC-responsive or background and comparison between two groups was carried out.

Reporting summary

Further information on research design is available in the Nature Portfolio Reporting Summary linked to this article.

Data availability

All data generated as part of this study is available through the Gene Expression Omnibus (GEO) database with accession number GSE147123.

Code availability

All code used as part of this study is available through GitHub (https://github.com/dixonlab/).

65. Ran, F. A. et al. Genome engineering using the CRISPR–Cas9 system. *Nat. Protoc.* **8**, 2281–2308 (2013).
66. DePristo, M. A. et al. A framework for variation discovery and genotyping using next-generation DNA sequencing data. *Nat. Genet.* **43**, 491–498 (2011).
67. Selvaraj, S., J, R. D., Bansal, V. & Ren, B. Whole-genome haplotype reconstruction using proximity-ligation and shotgun sequencing. *Nat. Biotechnol.* **31**, 1111–1118 (2013).
68. Edge, P., Bafna, V. & Bansal, V. HapCUT2: robust and accurate haplotype assembly for diverse sequencing technologies. *Genome Res.* **27**, 801–812 (2017).
69. Dobin, A. et al. STAR: ultrafast universal RNA-seq aligner. *Bioinformatics* **29**, 15–21 (2013).

70. Anders, S., Pyl, P. T. & Huber, W. HTSeq–a Python framework to work with high-throughput sequencing data. *Bioinformatics* **31**, 166–169 (2015).
71. Haas, B. J. et al. Accuracy assessment of fusion transcript detection via read-mapping and de novo fusion transcript assembly-based methods. *Genome Biol.* **20**, 213 (2019).
72. Li, H. Aligning sequence reads, clone sequences and assembly contigs with BWA-MEM. Preprint at https://arxiv.org/abs/1303.3997 (2013).
73. Imakaev, M. et al. Iterative correction of Hi-C data reveals hallmarks of chromosome organization. *Nat. Methods* **9**, 999–1003 (2012).
74. Consortium, I. T. P.-C. A. o. W. G. Pan-cancer analysis of whole genomes. *Nature* **578**, 82–93 (2020).
75. Nakamura, Y. et al. Targeting of super-enhancers and mutant BRAF can suppress growth of BRAF-mutant colon cancer cells via repression of MAPK signaling pathway. *Cancer Lett.* **402**, 100–109 (2017).
76. Diaferia, G. R. et al. Dissection of transcriptional and cis-regulatory control of differentiation in human pancreatic cancer. *EMBO J.* **35**, 595–617 (2016).
77. Abraham, B. J. et al. Small genomic insertions form enhancers that misregulate oncogenes. *Nat. Commun.* **8**, 14385 (2017).
78. Kalender Atak, Z. et al. Identification of cis-regulatory mutations generating de novo edges in personalized cancer gene regulatory networks. *Genome Med.* **9**, 80 (2017).
79. Ryan, R. J. et al. Detection of enhancer-associated rearrangements reveals mechanisms of oncogene dysregulation in B-cell lymphoma. *Cancer Discov.* **5**, 1058–1071 (2015).
80. Perreault, A. A., Sprunger, D. M. & Venters, B. J. Epigenetic and transcriptional profiling of triple negative breast cancer. *Sci. Data* **6**, 190033 (2019).
81. Franco, H. L. et al. Enhancer transcription reveals subtype-specific gene expression programs controlling breast cancer pathogenesis. *Genome Res.* **28**, 159–170 (2018).
82. Wang, Y. et al. CDK7-dependent transcriptional addiction in triple-negative breast cancer. *Cell* **163**, 174–186 (2015).
83. Feld, C. et al. Combined cistrome and transcriptome analysis of SKI in AML cells identifies SKI as a co-repressor for RUNX1. *Nucleic Acids Res.* **46**, 3412–3428 (2018).
84. Singh, A. A. et al. Optimized ChIP-seq method facilitates transcription factor profiling in human tumors. *Life Sci. Alliance* **2**, e201800115 (2019).
85. Liu, N. Q. et al. The non-coding variant rs1800734 enhances DCLK3 expression through long-range interaction and promotes colorectal cancer progression. *Nat. Commun.* **8**, 14418 (2017).
86. Wan, L. et al. ENL links histone acetylation to oncogenic gene expression in acute myeloid leukaemia. *Nature* **543**, 265–269 (2017).
87. Saito, S. et al. Eradication of central nervous system leukemia of T-cell origin with a brain-permeable LSD1 inhibitor. *Clin. Cancer Res.* **25**, 1601–1611 (2019).
88. Mansour, M. R. et al. Oncogene regulation. An oncogenic super-enhancer formed through somatic mutation of a noncoding intergenic element. *Science* **346**, 1373–1377 (2014).
89. Eliades, P. et al. High MITF expression is associated with super-enhancers and suppressed by CDK7 inhibition in melanoma. *J. Invest. Dermatol.* **138**, 1582–1590 (2018).
90. Boeva, V. et al. Heterogeneity of neuroblastoma cell identity defined by transcriptional circuitries. *Nat. Genet.* **49**, 1408–1413 (2017).
91. Cohen, A. J. et al. Hotspots of aberrant enhancer activity punctuate the colorectal cancer epigenome. *Nat. Commun.* **8**, 14400 (2017).
92. Valenciaga, A. et al. Transcriptional targeting of oncogene addiction in medullary thyroid cancer. *JCI Insight* **3**, e122225 (2018).
93. Chen, P. et al. Symbiotic macrophage-glioma cell interactions reveal synthetic lethality in PTEN-null glioma. *Cancer Cell* **35**, 868–884 e866 (2019).
94. Zhang, Y. et al. Model-based analysis of ChIP-Seq (MACS). *Genome Biol.* **9**, R137 (2008).
95. Adrian Alexa, J. R. topGO: Enrichment analysis for gene ontology. R package version 2.48.0 https://doi.org/10.18129/B9.bioc.topGO (2022).

Acknowledgements We thank A. Saghatelian and A. Deshpande for contributing cell lines to this study. We thank A. Kim for sharing the mCherry modified version of the pX458 plasmid. We thank T. Popay for helpful comments on the manuscript. This work was supported by the NIH grant DP5OD023071 to J.R.D. and is also supported by the Leona M. and Harry B. Helmsley Charitable Trust grant No. 2017-PG-MED001 to J.R.D. Work in the laboratory of G.M.W. was supported, in part, by the National Institutes of Health/National Cancer Institute (grant no. R35 CA197687) and the Breast Cancer Research Foundation (BCRF). This work was also supported by the Flow Cytometry Core Facility of the Salk Institute and the NGS Core Facility of the Salk Institute with funding from NIH-NCI CCSG (grant no. P30 014195). We thank UC San Diego Biorepository and Tissue technology who shared resources for Biospecimen collection. This work carried out at the UC San Diego Moore's Cancer Center Comprehensive Biorepository was supported by the National Cancer Institute (grant no. NCI P30CA23100).

Author contributions Z.X., D.-S.L. and J.R.D. conceived and designed the study. Z.X., V.T.L., R.B., S.C., J.Y., S.D., S.M., B.C., N.H, C.Y.C, S.T. and J.R.D. conducted the experiments. D.-S.L., Z.X. and J.R.D. led the data analysis. K.C.A. and P.A.F. contributed to the analysis of structural variation in patient tumour samples. G.M.W. and G.M. contributed to and helped supervise the experimental design. Z.X., D.-S.L. and J.R.D. wrote the manuscript. All authors read and approved the manuscript.

Competing interests The authors declare no competing interests

Additional information

Supplementary information The online version contains supplementary material available at https://doi.org/10.1038/s41586-022-05504-4.

Correspondence and requests for materials should be addressed to Jesse R. Dixon.

Peer review information *Nature* thanks Charles Lin, Ekta Khurana and the other, anonymous, reviewer(s) for their contribution to the peer review of this work.

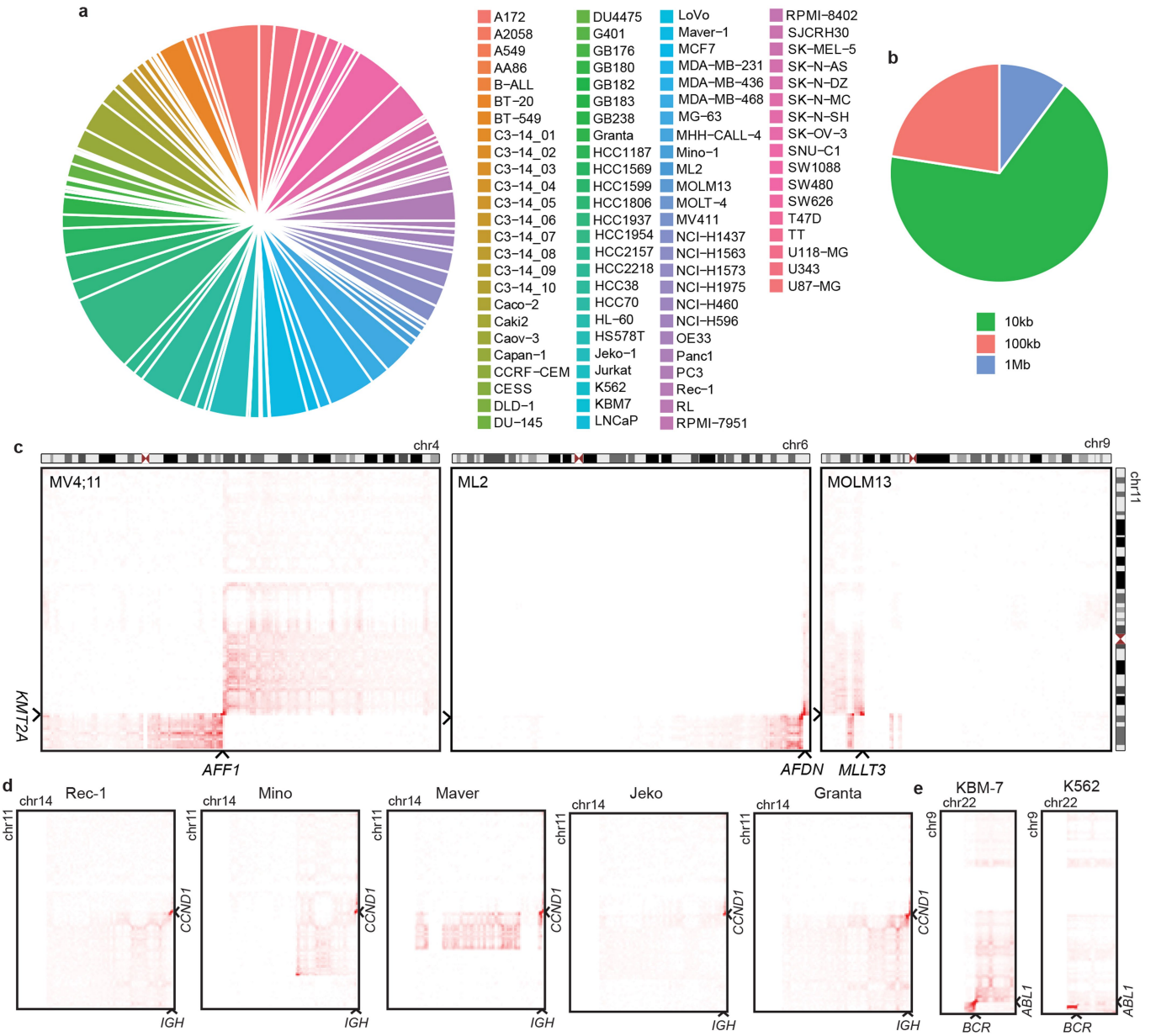

Extended Data Fig. 1 | Identification of rearrangements based on Hi-C data. **a**, Pie chart showing all 4,543 rearrangements identified and which cell line or patient tumor sample they are derived from. The order in the pie chart starts with A172 cells and proceeds counter-clockwise. **b**, Resolution of structural variants calls from Hi-C. Calls are first identified at low resolution and then progressively refined. The resolution reported is the highest resolution with which a given structural variant is identified. **c**, Chromatin interaction maps from mixed lineage leukemia cell lines with known MLL/*KMT2A* rearrangements. The maps show the presence of translocations on chromosome 4 in MV4;11 cells (left), chromosome 6 in ML2 cells (middle), and chromosome 9 in MOLM13 cells (right). **d**, Heat maps showing known disease defining translocations from five Mantle Cell lymphoma cell lines (Rec-1, Mino, Maver, Jeko, Granta). **e**, Heat maps showing known disease defining translocations in two Chronic Lymphocytic Leukemia cell lines (K562 and KBM7).

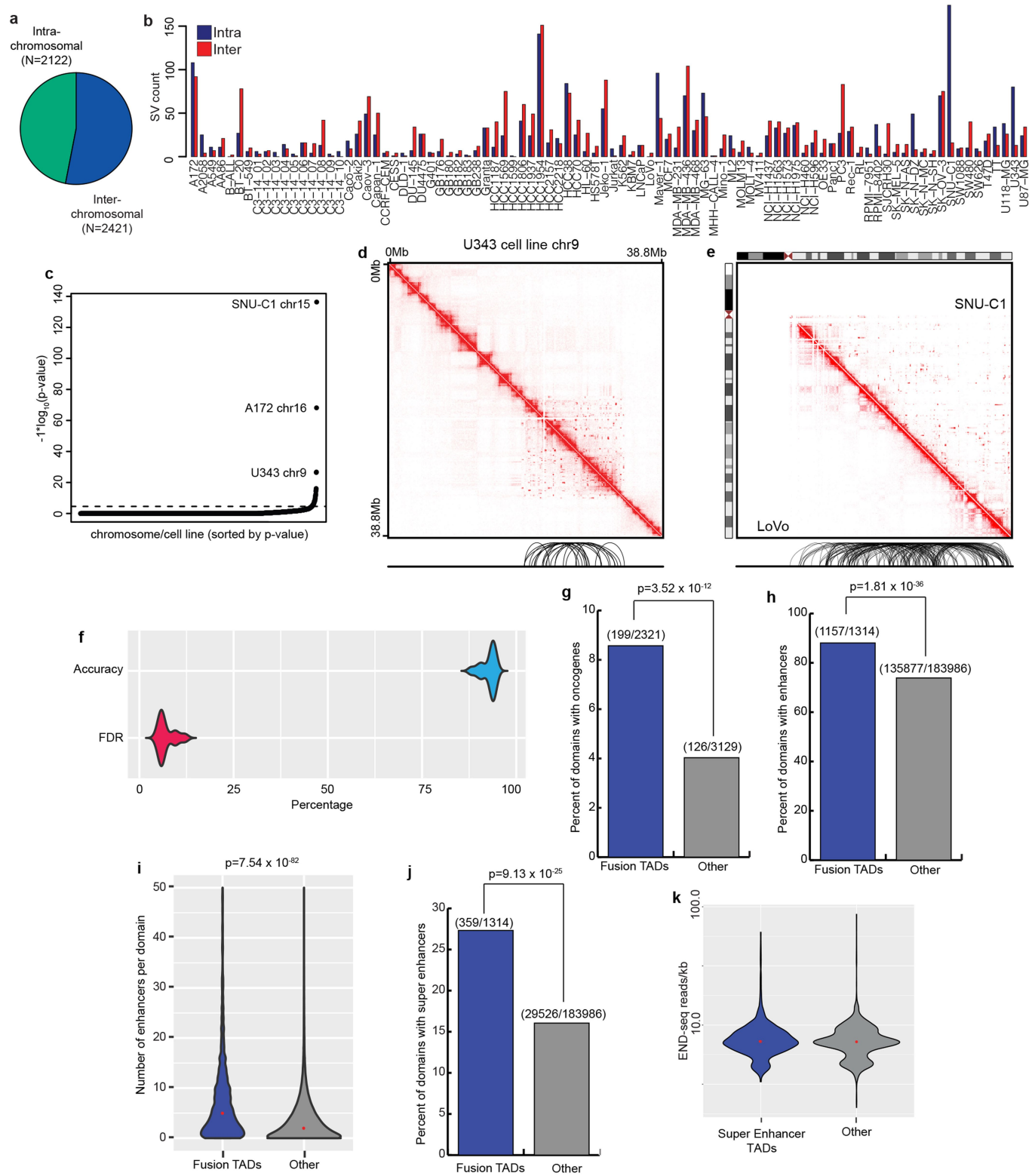

Extended Data Fig. 2 | See next page for caption.

Extended Data Fig. 2 | Features associated with TAD fusion events. a, Pie chart showing the fraction of intra-chromosomal vs. inter-chromosomal structural variant predictions. **b**, The number of observed intra-chromosomal (blue) or inter-chromosomal (red) rearrangements identified in each cell line. **c**, $-\log_{10}$ (p-values) for the observed frequency of intra-chromosomal rearrangements for each chromosome in each cell line under the null hypothesis that rearrangements are randomly distributed across chromosomes. The dashed line shows the threshold for significance accounting for multiple testing using a Bonferroni correction ($p = 2.5 \times 10^{-5}$). **d**, Example of high-frequency local rearrangements on chromosome 9 in U343 cells. Below the matrix is an arc plot of predicted rearrangements. **e**, Example of high-frequency local rearrangements along chromosome 15 in SNU-C1 cells (shown in the upper right-hand half of the matrix) in comparison with data from chromosome 15 in LoVo cells (lower left hand) where no rearrangements are observed. Below the matrix is an arc plot of predicted rearrangements. **f**, Results of cross validation of the neural network. The violin plots show the distribution of the accuracy and false discovery rate (FDR) across all 82 samples. **g**, Bar plots showing the percentage of domains containing oncogenes (based on the Cosmic Cancer Gene census) in domains identified as being part of fusion TADs (blue) versus those not identified in fusion TADs (grey). P-value is calculated by Fisher's exact test. **h**, Bar plots showing the percentage of domains that contain enhancers for domains that contain TAD fusion events (blue) or do not (gray). The domain/enhancer analysis was performed for each domain in each cell type. P-value is calculated by Fisher's exact test. **i**, Violin plots showing the distribution of the frequency of enhancers in domains that show TAD fusion events (blue) versus those that do not (gray). P-value is calculated from the two-sided Wilcoxon Rank Sum test. **j**, Bar plots showing the percentage of domains that contain super enhancers for domains that contain TAD fusion events (blue) or do not (gray). The domain/super-enhancer analysis was performed for each domain in each cell type. P-value is calculated by Fisher's exact test. **k**, Violin plots showing the number of END-seq reads per kb for TADs that contain super enhancers (blue) versus those that do not (gray).

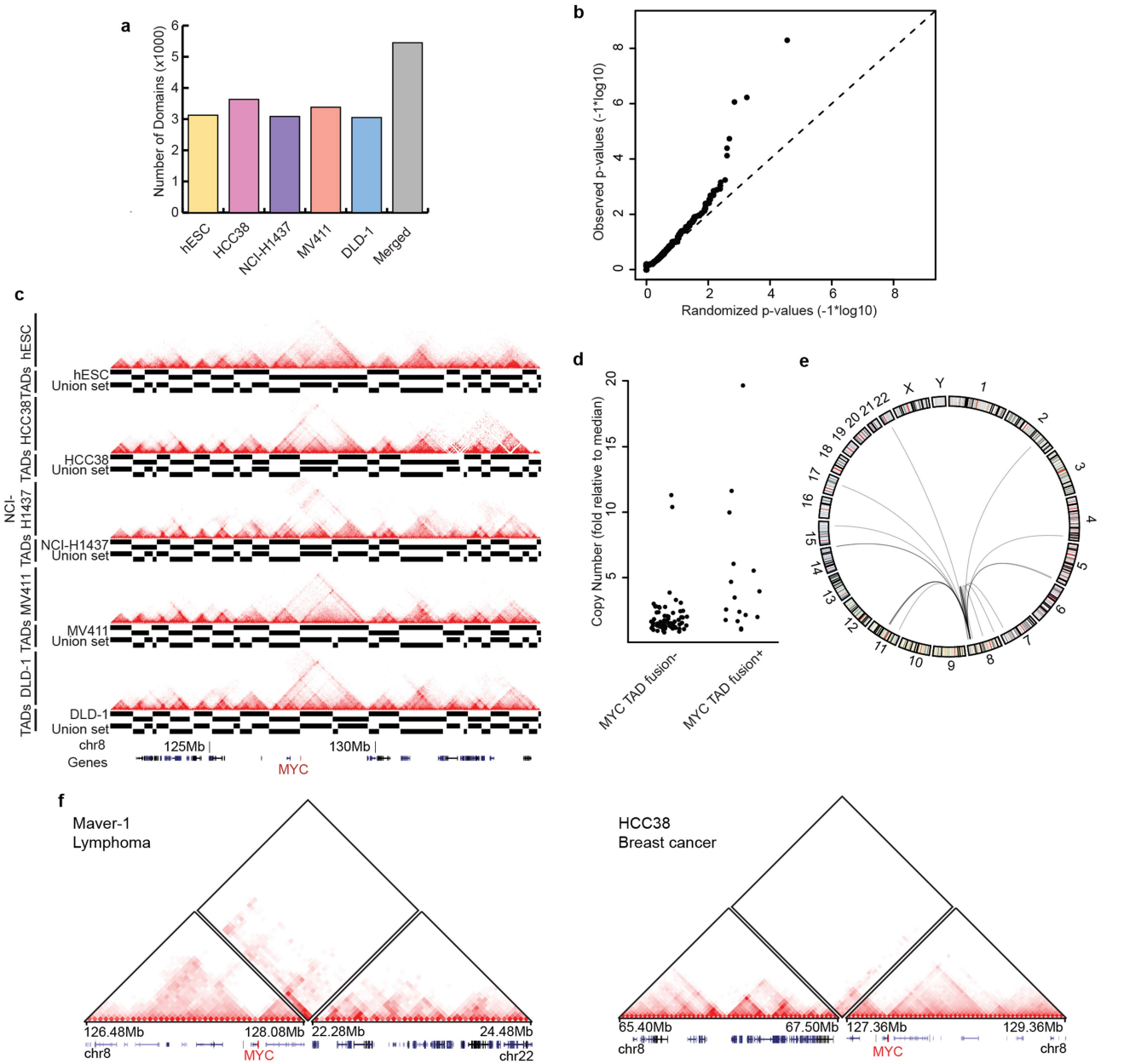

Extended Data Fig. 3 | TAD fusion events at the MYC locus. a, The number of called domains in each of five cell lines (hESC, HCC38, MV411, NCI-H1437, DLD-1) and the number of domains after merging unique boundaries (Merged). **b**, Quantile-quantile plot for evaluating the false discovery rate for recurrent TAD fusion identification. The observed p-values (Y-axis) are estimated using a Poisson model accounting for the overall frequency of rearrangements and the size of the domain. Randomized p-values are generated from these expected values (x-axis). This randomization analysis was repeated 1000 times to estimate the FDR at different p-value cut-offs. **c**, Hi-C data over the *MYC* locus in five cell types used for generating the merged TAD boundary set. The locations of TAD calls are shown in black bars below each heat map. This includes the TAD calls for each cell type as well as the across-cell merged calls ("Union set"). **d**, Estimated copy number of the *MYC* gene for samples with a TAD fusion event at the *MYC* locus versus those that do not. The copy number is estimated from the total number of Hi-C reads over the 100 kb bin surrounding the MYC gene divided by the median read count per 100 kb bin in each cell line. **e**, Circos plot showing the translocation partner region of each predicted TAD fusion event at the *MYC* locus. **f**, Examples of identified TAD fusion events at the *MYC* locus in two cell lines.

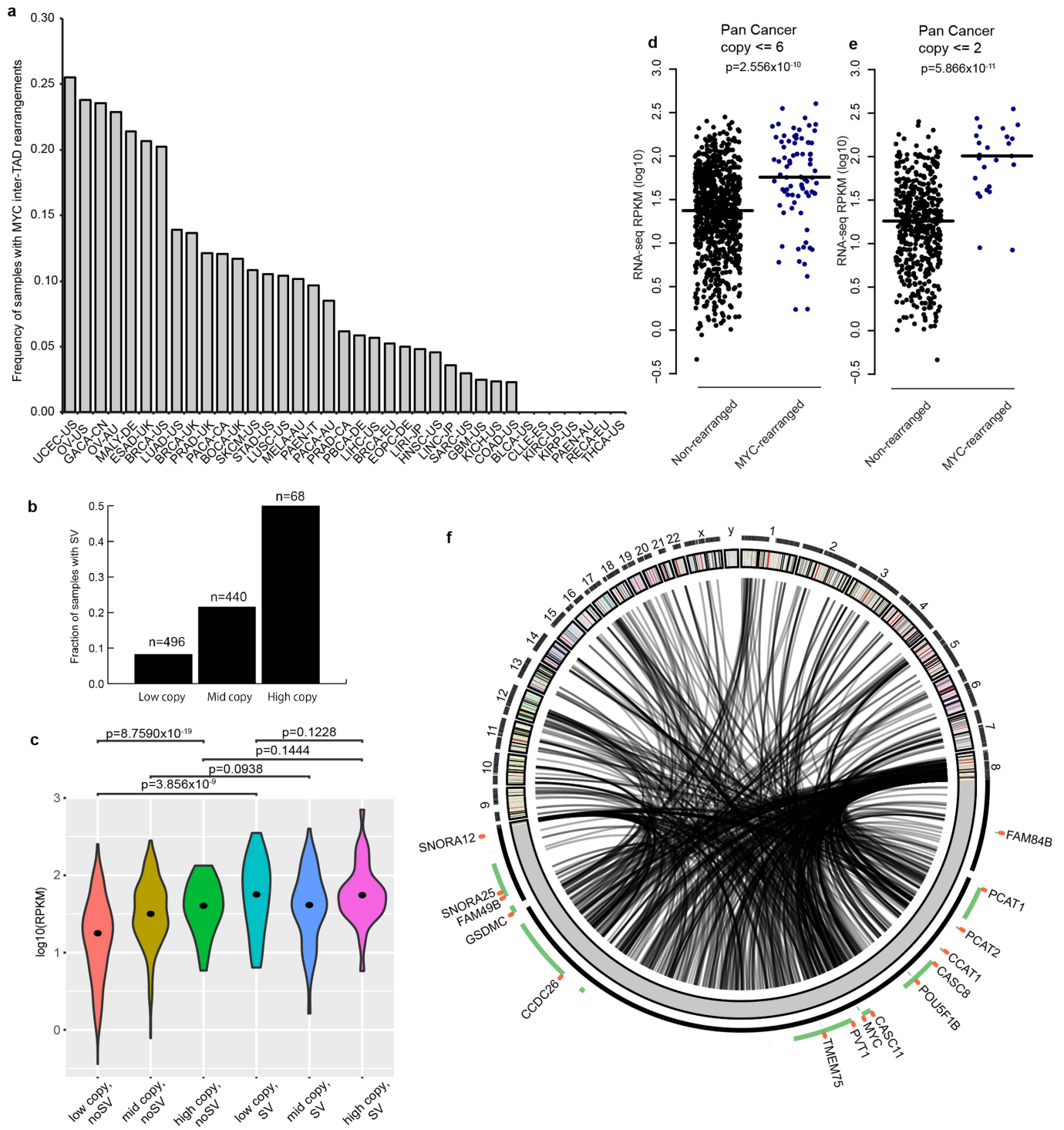

Extended Data Fig. 4 | Inter TAD rearrangements at the *MYC* locus in human patient tumor samples. a, Bar plot showing the frequency of patient samples containing inter-TAD rearrangements at the *MYC* locus by tumor type. **b**, Fraction of PCAWG samples with SVs at the *MYC* locus based on copy number. Samples are stratified into low copy (<=2), mid-copy (>2 and <=6), and high-copy (>6). **c**, Violin plots showing *MYC* expression for PCAWG samples stratified by copy number and the presence or absence of an SV at the *MYC* locus. P-values are calculated using Kruskal-Wallis test. **d**, RNA-seq expression of the *MYC* gene from patient samples with matched structural variant calls for samples with no high-level copy number alterations at the *MYC* gene (copy <= 6). Samples are separated into those that contain an inter-TAD rearrangement at the *MYC* locus (blue) and those that do not (black). P-value is from two-sided Wilcoxon Rank Sum test. **e**, RNA-seq expression of the *MYC* gene from patient samples with matched structural variant calls that are copy neutral at the *MYC* gene (copy <= 2). Samples are separated into those that contain an inter-TAD rearrangement at the *MYC* locus (blue) and those that do not (black). P-value is from two-sided Wilcoxon Rank Sum test. **f**, Circos plot of all inter-TAD rearrangements at the *MYC* locus. The Circos plot is zoomed in on cytoband 8q24.21 to show the *MYC* locus at a higher resolution. The position of TAD calls (black) and genes (green) are marked below the track.

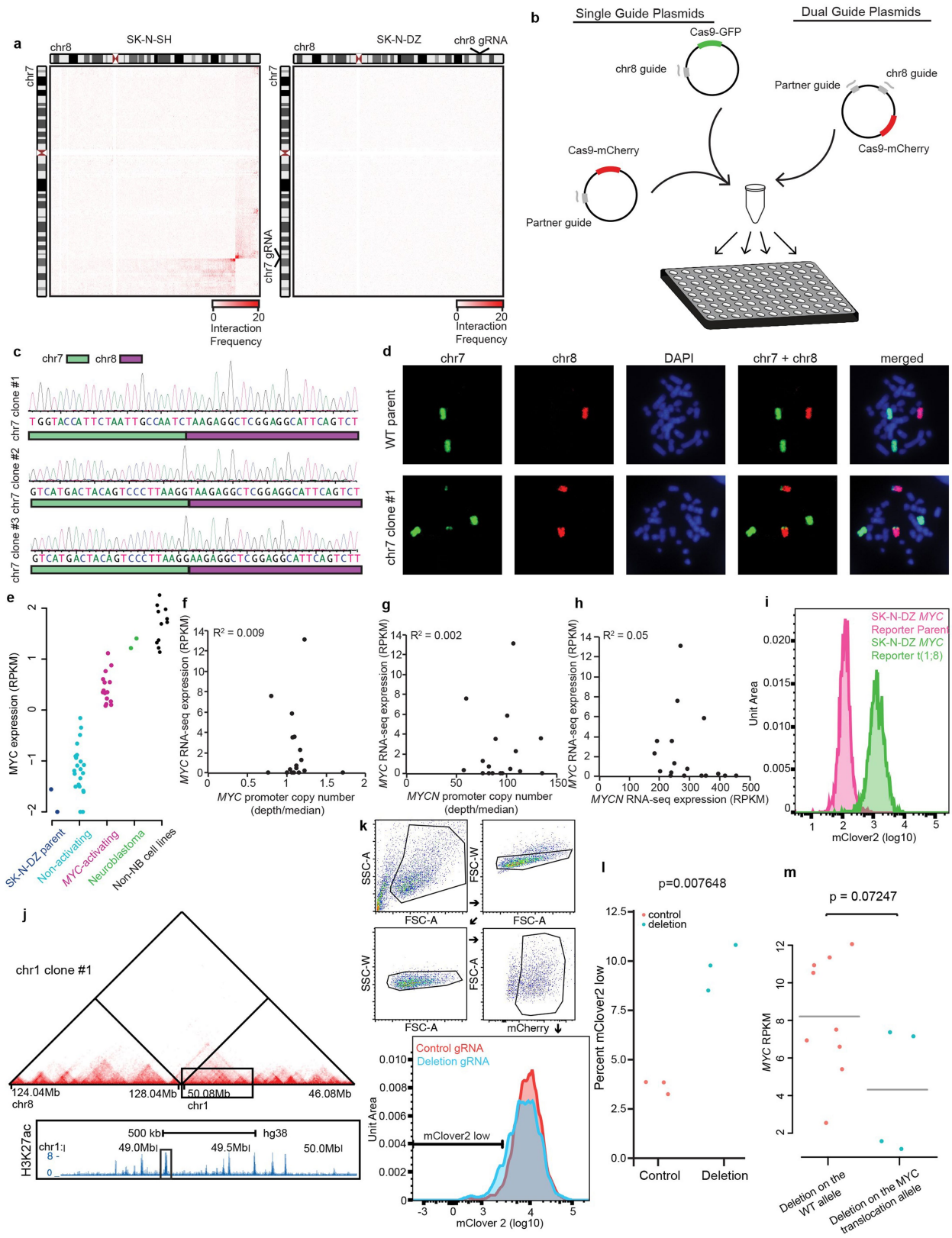

Extended Data Fig. 5 | See next page for caption.

Extended Data Fig. 5 | Engineered rearrangements in SK-N-DZ cells. a, Hi-C heat maps between chromosomes 7 and 8 in SK-N-SH cells (left) and SK-N-DZ cells (right). SK-N-SH cells have an endogenous t(7;8) translocation that creates a TAD fusion event at the locus, while SK-N-DZ cells have no rearrangements at the *MYC* locus in wild-type cells. **b**, Schematic for engineering rearrangement strategy. Guide RNAs targeting a locus ~300 kb downstream from the *MYC* gene and Guide RNAs targeting the partner region are cloned into a vector expressing Cas9. Guides are expressed either as single guides on plasmid with different fluorescent proteins or as dual guides on a plasmid with a single fluorescent protein. Cells are sorted and plated as single cells into 96 well plates. These can then be screened by PCR over the potential breakpoint to identify engineered clones. **c**, Sanger sequencing of PCR products from different engineered clones. The sequences that align to chromosome 7 are highlighted in green, while the sequences that align to chromosome 8 are highlighted in purple. **d**, Similar to Fig. 4b, validation of the engineered t(7;8) translocation by chromosome painting. **e**, *MYC* expression in cell lines containing endogenous or engineered rearrangements at the *MYC* locus including the non-rearranged SK-N-DZ parent cell line (purple), engineered clones classified as "Non-activating" (light blue), engineered clones classified as "*MYC*-activating" (dark red), Neuroblastoma cell lines with endogenous *MYC* rearrangements (green), and non-Neuroblastoma cell lines with *MYC* rearrangements (black). **f**, Scatter plot showing *MYC* expression (y-axis) and estimated *MYC* copy number (x-axis). **g**, Scatter plot showing *MYC* expression (y-axis) and estimated *MYCN* copy number (x-axis). **h**, Scatter plot showing *MYC* expression (y-axis) and *MYCN* expression (x-axis). **i**, FACS plots of mClover2 fluorescence in SK-N-DZ cells with a T2A-mClover2 reporter knocked into the 3′ end of the *MYC* gene (pink) and in a line derived from this *MYC* reporter with an engineered translocation between chromosome 1 and 8 (green). **j**, Heat map of chromosome 1 translocation to chromosome 8 with box showing H3K27ac ChIP-seq data over the partner region. The small inset box on the ChIP-seq track shows the enhancer targeted for deletion. **k**, FACS showing mClover2 fluorescence levels in the original chromosome 1 and chromosome 8 *MYC* reporter translocation (red) and in the same line with the targeted enhancer deletion (blue). The gate shows the region classified as "mClover2 low". An example of the gating strategy for is also shown, including gating for single-cells and mCherry positive cells (FSC – forward scatter, SSC – side scatter, A – area, W – width). **l**, Percentage of "mClover2 low" cells in the control (red) and deletion (blue) cells. P-value is using Student's two-sided T-test. **m**, *MYC* RPKM of clones with enhancer deletion on wild type allele and *MYC*-translocated allele. P-value is using two-sided T-test with equal variance.

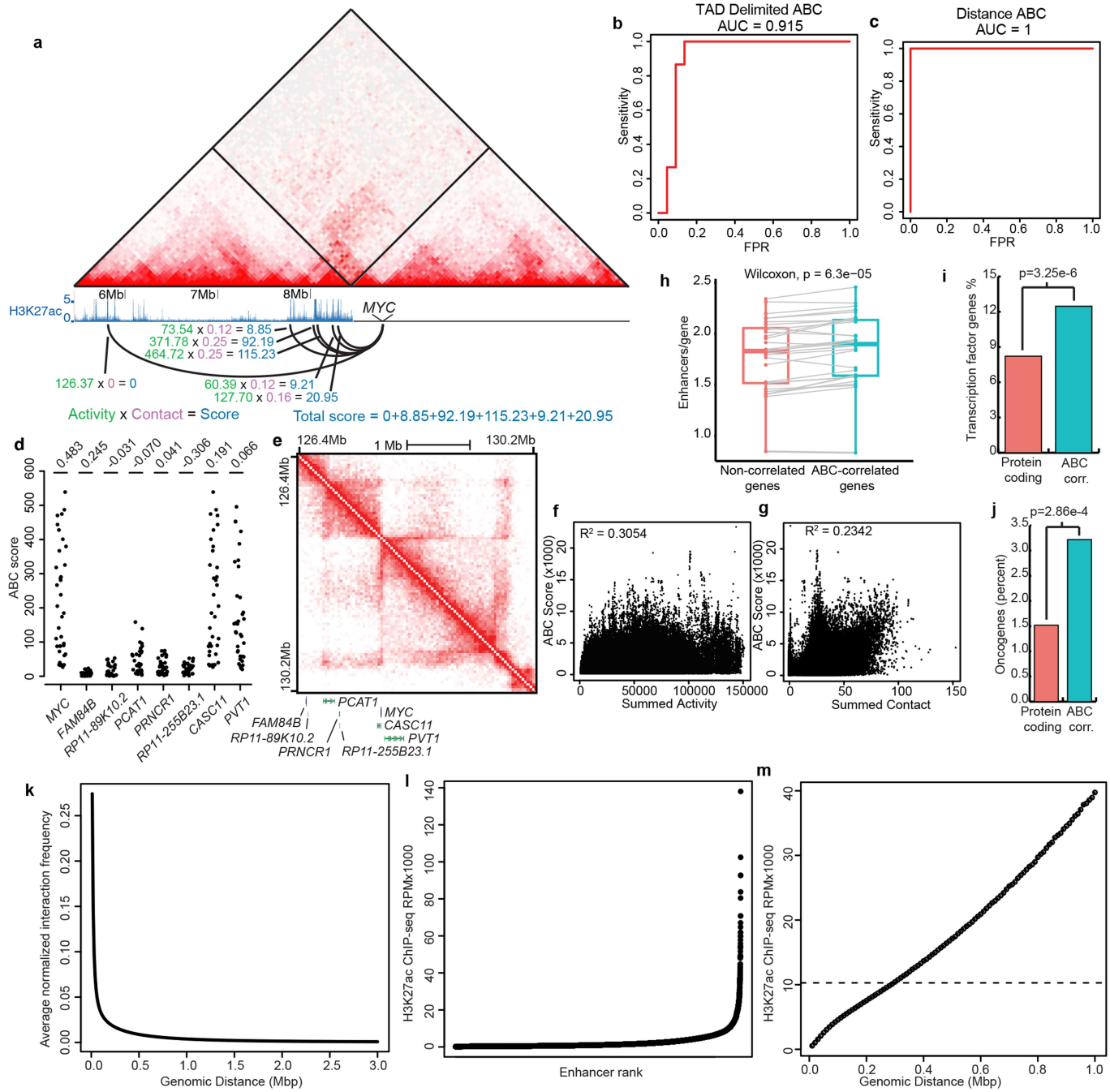

Extended Data Fig. 6 | See next page for caption.

Extended Data Fig. 6 | Models for activation in engineered rearrangements. **a**, Example plot showing method for calculating ABC score for *MYC* with rearranged partner sites. Interaction frequency between the *MYC* promoter and H3K27ac peaks in the partner region ("contact") is multiplied by the strength of the H3K27ac signal ("activity") at each peak across the partner region to obtain a final score for each peak. This signal is then summed across all peaks over the partner region. Of note, this example plot only shows the calculations for the six strongest H3K27ac peaks in the partner region, whereas the actual score is calculated using all H3K27ac peaks. **b**, Receiver Operating Characteristic (ROC) curve for the TAD delimited ABC model. Shown above the plot is the area under the curve (AUC). **c**, ROC curve for an ABC model where contacts are measured from genome wide average interaction frequencies. **d**, Plots showing ABC scores for genes neighboring *MYC*. Above the plot is the Pearson correlation coefficient for each gene between the genes' ABC score and expression. **e**, Heat map of the TAD surrounding *MYC* as well as the location and relative position of the genes shown in panel D. **f**, Scatter plot showing ABC scores and summed enhancer activity within 3 Mb for every gene in 30 cancer cell lines. **g**, Scatter plot showing ABC scores and summed interaction within 3 Mb for every gene in 30 cancer cell lines. **h**, The number of enhancers per gene linked by the marginal ABC score >= 0.1 for ABC-correlated and non-correlated genes. Gray lines show the paired values for each cell line comparing ABC-correlated and non-correlated genes. P-value is from paired Wilcoxon test. **i**, Percentage of ABC responsive (blue) and protein-coding genes classified as transcription factors. Protein coding genes are from the Gencode reference annotation. P-value is from Fisher's Exact test. **j**, Percentage of ABC responsive (blue) and protein-coding genes classified as oncogenes according to the Cosmic cancer gene census. P-value is from Fisher's Exact test. **k**, Normalized interaction frequency as a function of distance for Hi-C interactions at 10 kb resolution in SK-N-DZ cells. Interaction frequency decays exponentially as a function of distance. **l**, Enhancer activity based on H3K27ac ChIP-seq as quantified by the ROSE super enhancer calling activity for all enhancers in SK-N-DZ cells. Enhancers are displayed ranked according to strength. Super-enhancers show exponentially stronger enhancer activity compared with typical enhancers. **m**, Enhancer activity required to achieve the equivalent activity-by-contact score for the median enhancer at 20 kb in SK-N-DZ cells as a function of genomic distance. Shown as a dashed line is the minimal enhancer strength categorized as a "super-enhancer" in SK-N-DZ cells by the ROSE algorithm. Due to the exponential decay in interaction frequency. After ~300 kb, the only enhancers capable of producing an ABC score equivalent to the median enhancer at 20 kb are super enhancers.